

1 **Breast MRI segmentation for density estimation: Do different methods give the**
2 **same results and how much do differences matter?**

3 Simon J. Doran,^{1, a)} John H. Hipwell,^{2, b)} Rachel Denholm,³ Björn Eiben,² Marta
4 Busana,³ David J. Hawkes,² Martin O. Leach,¹ and Isabel dos Santos Silva³

5 ¹⁾*Cancer Research UK Cancer Imaging Centre, Division of Radiotherapy*
6 *and Imaging, The Institute of Cancer Research, London, SM2 5NG,*
7 *UK.*

8 ²⁾*Centre for Medical Image Computing (CMIC), Department of*
9 *Medical Physics and Bioengineering, UCL, London, WC1E 7JE,*
10 *UK.*

11 ³⁾*Department of Non-Communicable Disease Epidemiology,*
12 *London School of Hygiene & Tropical Medicine, London, WC1E 7HT,*
13 *UK.*

14 (Dated: 24 April 2017)

ABSTRACT

Purpose To compare two methods of automatic breast segmentation with each other and with manual segmentation in a large subject cohort. To discuss the factors involved in selecting the most appropriate algorithm for automatic segmentation and, in particular, to investigate the appropriateness of overlap measures (e.g., Dice and Jaccard coefficients) as the primary determinant in algorithm selection.

Methods Two methods of breast segmentation were applied to the task of calculating MRI breast density in 200 subjects drawn from the Avon Longitudinal Study of Parents and Children, a large cohort study with an MRI component.

A semi-automated, bias-corrected, fuzzy C-means (BC-FCM) method was combined with morphological operations to segment the overall breast volume from in-phase Dixon images. The method makes use of novel, problem-specific insights. The resulting segmentation mask was then applied to the corresponding Dixon water and fat images, which were combined to give Dixon MRI density values. Contemporaneously acquired T_1 - and T_2 -weighted image datasets were analysed using a novel and fully automated algorithm involving image filtering, landmark identification and explicit location of the pectoral muscle boundary. Within the region found, fat-water discrimination was performed using an Expectation Maximisation - Markov Random Field technique, yielding a second independent estimate of MRI density.

Results Images are presented for two individual women, demonstrating how the difficulty of the problem is highly subject-specific. Dice and Jaccard coefficients comparing the semiautomated BC-FCM method, operating on Dixon source data, with expert manual segmentation are presented. The corresponding results for the method based on T_1 - and T_2 -weighted data are slightly lower in the individual cases shown, but scatter plots and inter-class correlations for the cohort as a whole show that both methods do an excellent job in segmenting and classifying breast tissue.

Conclusions Epidemiological results demonstrate that both methods of automated segmentation are suitable for the chosen application and that it is important to consider a range of factors when choosing a segmentation algorithm, rather than focus narrowly on a single metric such as the Dice coefficient.

PACS numbers: 87.61.-c, 87.19.xj, 87.57.C-, 87.57.N-

Keywords: breast cancer, MRI, mammographic density, ALSPAC, segmentation

^{a)} Joint first author and corresponding author: Simon.Doran@icr.ac.uk

^{b)} Joint first author: j.hipwell@ucl.ac.uk

17 I. INTRODUCTION

18 Mammographic density, a quantitative measure of radio-dense fibroglandular tissue in the
19 breast, is one of the strongest predictors of breast cancer risk. Women with more than 75%
20 density have a four-fold or higher risk of breast cancer compared to those with less than 5%¹.
21 More intensive screening for women with high mammographic density has been proposed²
22 but remains controversial³.

23 However, in clinical practice, mammographic density, as assessed on x-ray mammograms,
24 is generally reported using only qualitative, radiologist-assessed categories, and agreement
25 between radiologists tends to be only moderate⁴. Quantitative analysis is hampered by the
26 fact that breast density is an inherently 3-D material property and therefore not well suited
27 to measurement using 2-D x-ray projections. Although subsequent risk assessment and epi-
28 demiological analysis rarely use full 3-D information (normally preferring a single number,
29 i.e., the volume-averaged mean breast density), accurate derivation of such a statistic from
30 the 2-D X-ray data is problematic and subject to error. Automated tools such as Volpara
31 (VolparaSolutions, Wellington, NZ)⁵ and QUANTRA (Hologic Inc., USA) are gaining trac-
32 tion in the mammography community, suggesting that mean breast density can be calculated
33 without inter-reader bias. However, such readings may be affected by errors in estimating
34 breast thickness⁶ and the relation between the values of breast density reported and those
35 obtained by other techniques remains to be elucidated⁷.

36 Increasingly, Magnetic Resonance Imaging (MRI) mammography is being used in clinical
37 and research settings to assess breast structure, because of its 3-D capabilities, its non-
38 ionizing nature and the strong soft tissue contrast between fibroglandular (parenchymal)
39 and fatty tissue. In an MRI context, breast density refers to the percentage of breast tissue
40 volume that is deemed to be “parenchymal” and this is generally assumed to be the same as
41 volume fraction of tissue whose MR signal arises from free water molecules, as opposed to
42 fat (i.e., the “water fraction” or “percentage water”). Clearly, this is not an exact equivalent
43 of the mammographic x-ray density. Nevertheless, Thompson *et al.*⁸ demonstrate a clear
44 correlation between the two.

45 At present manual evaluation of MRI 3-D breast density is an arduous, observer-
46 dependent, and time-consuming process. Therefore, full or partial automation of the 3-D
47 analysis of the breast is required. To achieve the desired segmentations of breast parenchy-

mal volume and breast fat volume, two separate image processing tasks are required. First, the breast as a whole needs to be distinguished from the background and chest wall; and, second, the parenchymal tissue within the breast needs to be distinguished from fat.

Several different MRI pulse sequences have previously been used to assess breast density, but no definitive consensus has been reached about which is optimal. Few studies have compared different sequences within the same subject population. Furthermore, whilst there is a large body of prior literature (see Table I) describing different ways to achieve the two segmentation tasks described above, no studies, to date, have compared different automated methods with each other and with manual segmentation, for a sizeable subject population.

It is clear that many methods can produce “good” segmentation results. This study poses the following question: Do the minor differences we see between segmentations when we apply different algorithms on the same data actually matter for the uses to which the segmentations are ultimately put?

This study compares two very different methods of breast-outline segmentation: (i) an established³⁷ bias-corrected fuzzy C-means (BC-FCM) clustering technique based on a cost-function; and (ii) a new heuristic approach based on thresholding, landmark identification and direct analysis of image features. The results of this part of the study will be measures of overall breast volume from each method and volume similarity measures (Dice and Jaccard coefficients).

With the breast outline obtained, the second part of the study compares two methods of fat-water discrimination, again based on different principles: (i) The Dixon approach³⁸ uses scans acquired with an MRI technique that returns separate “fat” and “water” images. In principle, these allow us to obtain a fat and water fraction for every voxel, accounting for partial volume effects. However, Dixon sequences are not currently part of the routine acquisition protocol for clinical MRI examinations³⁹. (ii) Our second method uses an analysis of the intensity histograms of the two different tissue classes in fat-suppressed T_1 -weighted (T1w) and T_2 -weighted (T2w) images. Such images are routinely acquired in diagnostic scanning and this method thus has the potential advantage of wider applicability if the two methods are shown to be concordant. Note that there is no means of obtaining ground truth data and, given that we are dealing with a healthy subject cohort, no possibility of obtaining x-ray data for comparison.

Nomenclature for the various segmentations is summarised in Figure 1.

TABLE I: Summary of journal papers describing methods to segment pectoral muscle and internal fibro-glandular tissue from MR images. N_{OB} refers to the number of observers who provided the gold standard manual segmentation. N_D indicates the number of MR data sets the method was validated with and N_S the number of MRI scanners. N/A = not applicable; N/S = not specified

| Author, Year | Ref. no. | Breast outline segmentation method | Fat / water classification method | N_{Obs} | N_D | N_S |
|-----------------------------------|----------------|--|-----------------------------------|-----------|-------|-------|
| Hayton <i>et al.</i> 1997 | 9 | Threshold, morphological opening followed by “dynamic programming” | None | N/S | 3 | N/S |
| Twellmann <i>et al.</i> 2005 | 10 | Median filtering; Otsu automated thresholding; morphological closing | None | N/S | 12 | 1 |
| Koenig <i>et al.</i> 2005 | 11 | Histogram-based threshold for breast-air, then Gaussian smoothing; intensity threshold for pectoral boundary, then min and max of locations with transition within confidence interval | None | N/S | 4 | N/S |
| Yao 2005 | 12 | Threshold, morphological opening and region-growing followed by Bernstein-spline and active contour; automatic identification of key points to define rough surfaces of pectoral muscle; successive refinement via gradient-based technique, Bernstein spline and active contour | Fuzzy C-means | 1 | 90 | N/S |
| Lu <i>et al.</i> 2006 | 13 | Region-growing, then spline and active contour for breast-air boundary; location of key points by geometry; identification of muscle slab, followed by spline | None | N/S | 1 | 1 |
| Giannini <i>et al.</i> 2010 | 14 | Region-growing, then spline and active contour | None | 2 | 12 | 2 |
| Wang L <i>et al.</i> 2012 | 15 | Hessian sheetness filter; 3-D connected component algorithm; intensity-based region-growing based on seed points automatically selected | None | 1 | 84 | 5 |
| Wu <i>et al.</i> 2012a,b, 2013a,b | 16,17 18,19 | Thresholding, morphological opening, contour extraction; three edge maps generated from original data and two non-linear filters; candidate selection; median filtering; dynamic time-warping; comparison between slices | Continuous Max-Flow | 1 | 60 | 4 |

TABLE I: continued (atlas-based methods)

| Author, Year | Ref. no. | Breast outline segmentation method | Fat / water classification method | N_{Obs} | N_D | N_S |
|--|------------------|---|--|------------------|----------|-------|
| Gubern-Mérida <i>et al.</i> 2011 | ²⁰ | Manually created atlas with 7 tissue classes; landmark detection | Bayesian atlas plus Markov Random Field regularisation | 1 | 27 | 1 |
| Gubern-Mérida <i>et al.</i> 2012, 2015 | ^{21,22} | Manually created atlas; sternum detection; N3 bias-field correction | EM algorithm with Gaussian mixture model | 3,4 | 27+23 | 1 |
| Gallego-Ortiz and Martel 2012 | ²³ | Atlas created from Dixon in-phase images via entropy-based groupwise registration; maximal phase congruency and Laplacian mapping | None | N/S | 500 | 1 |
| Khalvati <i>et al.</i> 2015 | ²⁴ | Atlas created by manual initialization of active contour algorithm, subsequently corrected manually | None | N/S | 400 + 17 | 3 |
| Gallego and Martel 2011 | ²⁵ | Atlas, statistical shape model | None | N/S | 415 | N/S |

TABLE I: continued (neural networks and fuzzy C-means)

| | | | | | |
|-----------------------------------|---|--|-----------------|------------|----------|
| Ertas <i>et al.</i> 2006, 2008 | ^{26,27} Breast air boundary: threshold; chest-wall: four cascaded cellular neural networks | 1 | 39 | N/S | N/S |
| Wang C-M <i>et al.</i> 2008 | ²⁸ Support vector machines | Support machines | vector | N/S | 1 |
| Wang Y <i>et al.</i> 2013 | ²⁹ Support vector machines acting on multiple sets of MR images with different contrast | Support machines | vector | N/S | 1 |
| Klifa <i>et al.</i> 2004, 2010 | ^{30,31} Fuzzy C-means | Fuzzy C-means | >1 | 30 | N/S |
| Yang <i>et al.</i> 2009 | ³² Kalman filter-based linear mixing; fuzzy C-means | Kalman based linear mixing | filter- N/S | 1 | 1 |
| Nie <i>et al.</i> 2008 | ³³ Fuzzy C-means; V-cut; skin-exclusion; B-spline; manual refinement via GUI | Fuzzy C-means | 3 | 11 | 1 |
| Sathya <i>et al.</i> 2012 | ³⁴ Fuzzy C-means; support vector machines | None | N/S | 1 | 1 |
| Lin <i>et al.</i> 2011 | ³⁵ Fuzzy C-means and B-spline fitting, building on ³³ , with inhomogeneity correction via N3 | Fuzzy C-means, typically with 6 clusters | C-means, with 6 | 30 | 1 |
| Lin <i>et al.</i> 2013 | ^{33,36} Template-based | As per ³⁵ | 1 | 30 | 1 |
| Ertas <i>et al.</i> 2016 | ³⁷ Bias-corrected FCM, followed by morphological opening and closing | None | 1 | 82 | 4 |
| This study | Bias-corrected FCM vs thresholding, landmark analysis | Dixon vs 3 T1w and T2w contrast | 3 | 200 | 1 |

80 A comprehensive epidemiological analysis of the relationship between breast composition
 81 and seven other physical, historical and lifestyle variables has been carried out for this cohort.
 82 Whilst the full report is beyond the scope of this study, we summarise the results and use
 83 them to discuss quantitatively the impact of differences between the various assessment
 84 methods on conducting reliable clinico-epidemiological studies.

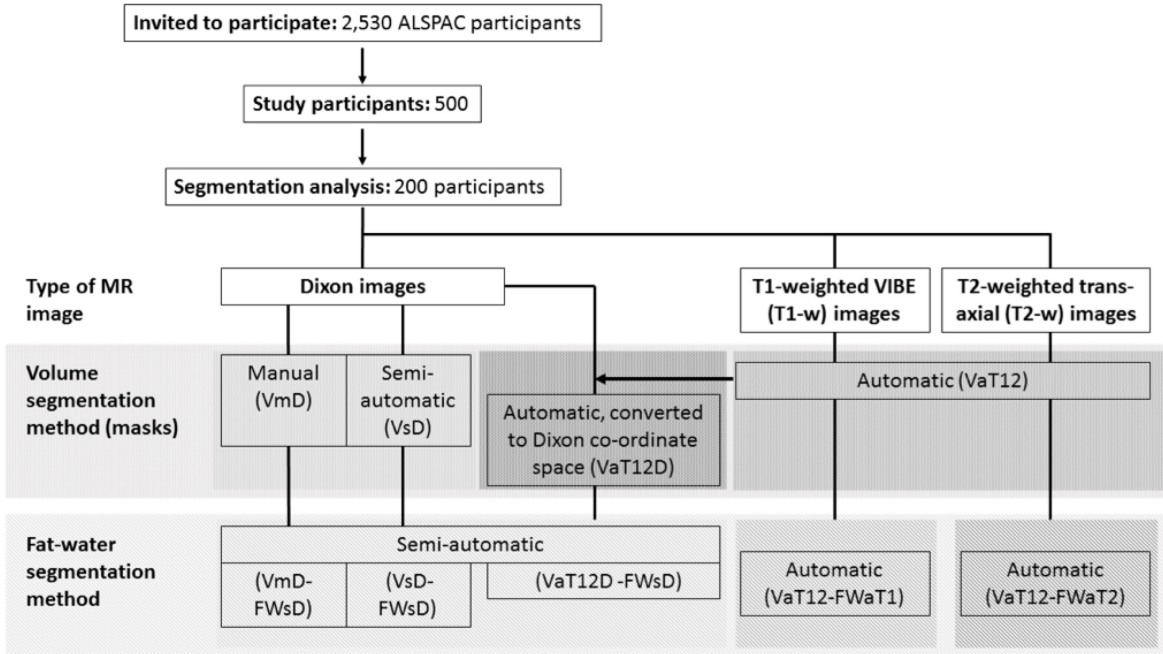


FIG. 1: Flow diagram of the overall data processing chain and nomenclature for the various segmentation methods. Some of these have the potential to operate on different source data and we can also combine the methods in different ways to achieve an overall result. We thus assign each step three codes: *segmentation purpose* (V = breast volume, FW = fat-water); *degree of automation* (m = manual, s = semi-automatic, a = fully automatic); and *source data* (D = Dixon; T_1 = T_1 -weighted, T_2 = T_2 -weighted, T_{12} = uses both T_1 - and T_2 -weighted data). Thus, a breast-volume measurement using semi-automatic segmentation on original Dixon data would be represented as VsD . Fat-water segmentations require both source data and a previously-generated volume mask, so are represented by the combination of two codes. For instance, fat-water statistics calculated semi-automatically from Dixon source data and using a mask generated automatically from T_1w and T_2w data would be described by VaT_{12} - $FWsD$. We note one additional case, in which the volume mask VaT_{12} is re-sampled to give a result in the same coordinate space as the Dixon images and we assign this the label $VaT_{12}D$.

85 II. METHODS

86 A. Data

87 1. *Study Population*

88 This work forms part of an investigation into breast composition at young ages, nested
 89 within the Avon Longitudinal Study of Parents and Children (ALSPAC). ALSPAC originally
 90 recruited 14,541 pregnant women resident in Avon, UK with expected dates of delivery 1st
 91 April 1991 to 31st December 1992, as described by Boyd *et al.* in a cohort profile paper⁴⁰. For
 92 this sub-study, Caucasian nulliparous women were invited to attend an MRI examination at
 93 the University of Bristol Clinical Research and Imaging Centre (CRIC) between June 2011
 94 and November 2014. Women were restricted to those from a singleton birth, who had never
 95 been diagnosed with a hormone-related disease and had regularly participated in follow-up
 96 surveys, including completing the age 20y questionnaire (2010-2011). Of the 2530 invited,
 97 500 (19.8%) eligible women attended.

98 The ALSPAC Law and Ethics Committee and the Local Research Ethics Committees
 99 gave ethical approval for the study. The study website contains details of all the data that
 100 are available through a fully searchable data dictionary⁴¹.

101 2. *MR Imaging*

102 Participants underwent a breast MRI scan using a 3T Siemens Skyra MR system with
 103 a breast coil that surrounds both breasts of a prone patient. Three sets of bilateral images
 104 were acquired:

- 105 • multislice, sagittal Dixon³⁸ images (in-phase, out-of-phase, water and fat), acquired
 106 using a turbo spin-echo sequence with nominal in-plane resolution of (0.742×0.742)
 107 mm^2 , nominal slice thickness 7 mm and interslice spacing 7.7 mm;
- 108 • T1-weighted 3D images, acquired using a VIBE sequence with fat saturation and
 109 a nominal resolution of $(0.759 \times 0.759 \times 0.900) \text{mm}^3$, as routinely used in clinical
 110 dynamic contrast-enhanced MRI protocols for the breast;
- 111 • multislice, axial, T2-weighted images, acquired using a turbo spin-echo sequence, with

112 nominal in-plane resolution of (0.848×0.848) mm², and both slice thickness and
113 spacing between slices 4 mm;

114 **3. *Manual Reference Segmentation***

115 To assess breast volume, a manual segmentation protocol (as described in the Supplemen-
116 tary Information) was developed and used by three readers (RD, MB and ISS) independently
117 to outline the breast from surrounding tissues in the Dixon images, using ITK-SNAP (ver-
118 sion 3.0.0). All subjects had a manual segmentation of all breast slices performed by at least
119 one reader. The datasets of 16 representative subjects were manually segmented twice by
120 all three readers to assess between- and within-observer variation. In cases where more than
121 one manual segmentation is performed, the VmD and VmD-FWsD results quoted below
122 represent the median values taken for the multiple manual readings.

123 **4. *Training and Validation Data Sets***

124 A training set of 100 randomly selected subjects was used to make initial comparisons
125 across MR images and segmentation methods, and for the manual readings, between- and
126 within-observer variation. The training data were used to assess the common reasons for
127 segmentation failure and to improve the algorithms. At the end of the testing phase, the
128 algorithm code was “frozen” and final comparisons of the segmentation methods were com-
129 pleted on a second set of images from a further 100 participants. Except where stated other-
130 wise, all the summary statistical results presented here come from this second, “validation”
131 cohort. For further details concerning statistical methods, please see the Supplementary
132 Information.

133 **B. Breast Outline Segmentation**

134 **1. *Semi-automated, bias-corrected fuzzy C-means (BC-FCM)***

135 A fuzzy C-means (FCM) algorithm was applied to the Dixon in-phase images. It has
136 the advantage that it can be modified to carry out a simultaneous intensity inhomogeneity
137 compensation, or bias-correction (BC), and this is potentially less expensive computationally

138 than a prefiltering operation⁴². The algorithms in this section were implemented using IDL
 139 (Harris Geospatial Systems, Melbourne, FL, USA) and run on a standard desktop computer.

140 The BC-FCM variant we implemented is described in³⁷. Formally, the algorithm does not
 141 require a training dataset and so is an unsupervised clustering algorithm. However, in prac-
 142 tice, some experience with the types of data involved can improve the results dramatically.
 143 Except for the local smoothness criterion (introduced by cost function γ in ref.³⁷ — see this
 144 publication for all other related notation), BC-FCM *per se* does not use any spatial infor-
 145 mation. Nevertheless, a “good” segmentation involves a number of problem-specific insights
 146 and the basic BC-FCM method above was enhanced by additional heuristic algorithms in
 147 the spatial domain, based on the results obtained with the training data.

148 *a. Initial parameters and iteration threshold* After some experimentation, $\beta(\mathbf{r})$ was set
 149 to 0.1 for all spatial locations and ϵ to 0.01. The two initial class centroids c_f were calculated
 150 by taking the mean of the slice being processed and adding a lower and an upper offset.
 151 These two offsets are adjustable parameters under user control. For many subjects — see the
 152 Results section for an example —, a single set of defaults performed extremely well. However,
 153 for a small subset of “difficult” cases — second example in Results —, user interaction was
 154 needed to try various combinations. As implemented here, on a standard desktop computer,
 155 running non-optimised software, it took around 2 mins. to run the segmentation algorithm
 156 on each 3-D dataset. Thus, this “trial and error” step was the most frustrating feature
 157 of the BC-FCM method in practice. Numerous coding and hardware improvements (e.g.,
 158 parallelisation) could be made to the prototype to improve the user experience, potentially
 159 allowing these adjustable parameters to be altered by simple slider controls with immediate
 160 feedback.

161 We observed an improvement in performance by allowing the algorithm to perform sep-
 162 arate BC-FCM classifications for segmenting the posterior of the breast from the chest wall
 163 and segmenting the anterior portion from air, then merging the two volumes. Furthermore,
 164 it was noted that the optimal offsets providing the initial class centroids were often differ-
 165 ent for these two segmentation problems. Thus, each dataset is split into two portions in
 166 an anterior-posterior (AP) direction and the BC-FCM algorithm applied twice per image
 167 slice. Given that the size of breasts varies, the position of the AP-split is also different for
 168 different datasets and this is handled automatically by having two passes through the entire
 169 algorithm with an automated choice of the AP-split position made after Pass 1.

170 *b. Morphological operations* The breast outlining task requires a definite boundary to
171 be drawn. Thus, it is not necessary to use the full membership function output of the
172 BC-FCM routine, and we arrange for the clustering to produce a binary image. This may
173 include some misclassified regions outside the breast and some “holes” inside the breast. To
174 remove the unwanted regions, 2D hole-filling followed by a 4-neighbourhood connectivity
175 search and object labelling is performed. The largest non-background object in each slice is
176 identified as the breast region and other smaller objects are removed from the binary image.
177 This exercise is repeated for all slices and these are then merged to form an approximate
178 breast volume.

179 Within this approximate breast volume, there may be some non-breast tissue segmented
180 for cases in which fatty breast tissue is connected to the chest and liver; and there may also
181 be some unsegmented breast tissue left for cases in which dense breast tissue is connected to
182 the chest wall muscles. To reduce these over- and under-segmentations, 3D morphological
183 image opening is performed, followed by closing using two cylindrical structuring elements
184 having the same radius of 3 voxels but different heights of 3 voxels and 25 voxels in the axial
185 direction. These parameters were found by experimentation during our previous study³⁷.

186 *c. Lateral cutoffs* The preceding steps in the process do an excellent job in segmenting
187 the anterior and posterior margins of the breast. However, there is no consensus in the
188 literature as to “where the breast stops” in the right-left and superior-inferior directions.
189 The extent of the breast is not directly delineated by any change in MRI contrast and the
190 required boundary may, indeed, be specific to the application of the imaging (e.g., when
191 comparing the MRI segmentation with the breast region compressed within the paddles
192 of a mammography system, the axilla region may be excluded entirely). Thus, based on
193 the consensus protocol (Appendix ??) reached by the three experienced readers, a heuristic
194 algorithm was developed, as described below. This additional truncation is derived entirely
195 from geometric considerations and boundaries are drawn without regard to image intensity,
196 which is in many cases the same on either side of the boundary.

197 Each breast is processed in turn. The stack of sagittal images segmented using BC-
198 FCM forms a pseudo 3-D dataset. From this dataset the transverse plane containing the
199 largest breast area is passed to a simple algorithm that extracts the air-breast interface as
200 a 1-D “breast profile”. (This geometry is illustrated as Figure S2 of the Supplementary
201 Information.) The profile is used to determine the position of the breast midpoint in a left-

202 right direction. Working outwards from this midpoint, we find the first position at which
 203 the absolute value of the gradient (approximated by the finite difference between adjacent
 204 voxels) of the breast profile rises above a threshold value, determined by experimentation.
 205 This indicates a change in angle of the skin surface from flat regions between and outside
 206 the breasts, to the side contour of the breast. A mask is applied to exclude all sagittal slices
 207 in the original dataset on either side of these changes in angle. (Typically, the “raw” output
 208 of the BC-FCM algorithm would include these.) Finally, a similar profile is generated for
 209 the superior-inferior direction and the upper and lower bounds of the breast are determined
 210 in each sagittal plane of the original data.

211 **2. Fully-automated, using T1w and T2w Images**

212 *a. Pre-Processing Processing (Bias-Field Correction)* A slowly varying bias-field,
 213 caused by inhomogeneities in the magnetic field during the MR acquisition, is a com-
 214 mon artefact of MR images. To correct this for the T1w and T2w images, we apply the
 215 “N4ITK” nonparametric non-uniform intensity normalization method⁴³. This is a refine-
 216 ment of the popular N3 algorithm which adopts a fast, robust B-spline fitting algorithm
 217 and a hierarchical, multi-scale, optimisation scheme (figures 2a and 2b).

218 *b. Breast Mask Segmentation* This novel, heuristic method, implemented using the
 219 Insight Toolkit⁴⁴, computes a whole breast mask using both the T1w and T2w images.
 220 In developing this automated approach, emphasis has been placed on limiting the number
 221 of empirically derived parameters and relying instead on detecting statistical or functional
 222 extrema. In this way we aim to make the method as widely applicable to variations in
 223 subjects and images as possible. The method comprises a number of distinct processing
 224 steps as follows.

- 225 1. The T2w image is resampled to match the resolution of the T1w image.
- 226 2. A grey-scale closing operation along each of the orthogonal axes, \mathbf{x} , \mathbf{y} and \mathbf{z} , is per-
 227 formed on the T2w image, to eliminate voids from the subsequent foreground segmen-
 228 tation. In this operation each voxel’s intensity, I_{T2w} , at index (i, j, k) is replaced by
 229 $I_{cT2w}(i, j, k)$ according to:

$$I_{cT2w}(i, j, k) = \min \left[\begin{aligned} & \min \left(\max_{0 \leq i_1 \leq i} I_{T2w}(i_1, j, k), \max_{i < i_2 < N_i} I_{T2w}(i_2, j, k) \right), \\ & \min \left(\max_{0 \leq j_1 \leq j} I_{T2w}(i, j_1, k), \max_{j < j_2 < N_j} I_{T2w}(i, j_2, k) \right), \\ & \min \left(\max_{0 \leq k_1 \leq k} I_{T2w}(i, j, k_1), \max_{k < k_2 < N_k} I_{T2w}(i, j, k_2) \right) \end{aligned} \right] \quad (1)$$

230 where N_i, N_j, N_k are the number of voxels along each axis.

231 3. The T1w image is rescaled to match the intensity range of the closed T2w image and
 232 the maximum of these two images, $I_{\text{MaxT1wT2w}}$, computed.

233 4. The foreground (i.e. the subject) is segmented from the background by thresholding,
 234 $I_{\text{MaxT1wT2w}}$. The threshold, t_{bg} , is computed via:

$$t_{\text{bg}} = \arg \max_I [F_{\text{dark}}(I) (F_{\text{CDT}}(I) - F_{\text{var}}(I))] \quad (2)$$

235 according to the following functional criteria:

236 • The background is assumed dark therefore the threshold should be close to zero:

$$F_{\text{dark}}(I) = 1 - \frac{I}{\max(I)} \quad (3)$$

237 • The frequency of voxel intensities in the background is higher than the foreground
 238 i.e. the background intensities form a distinctive peak in the image histogram,
 239 $P(I)$, which is captured by a sharp rise in the cumulative intensity distribution
 240 function:

$$F_{\text{CDT}}(I) = \frac{\sum_{j=0}^I P(j)}{\sum_{k=0}^{\max(I)} P(k)} \quad (4)$$

241 • The background has a lower intensity variance than the foreground:

$$F_{\text{var}}(I) = \frac{\sum_{j=0}^I P(j)(j - \mu)^2}{\sum_{k=0}^{\max(I)} P(k)(k - \mu)^2} \quad (5)$$

242 The resulting foreground mask image is denoted I_{fg} — see Figure 2(d).

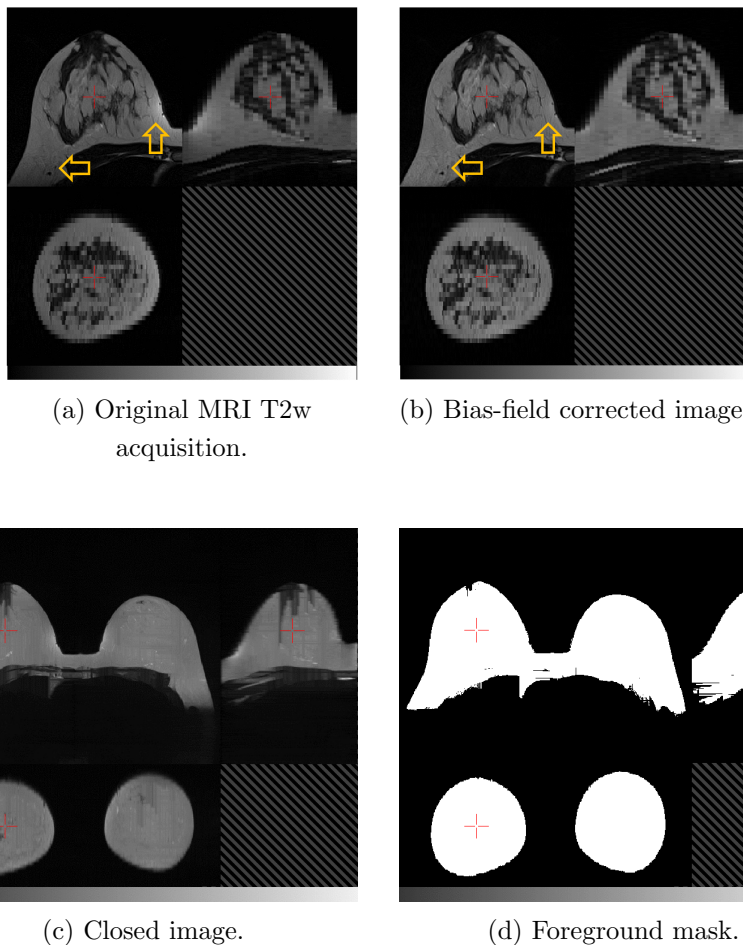


FIG. 2: Orthogonal slices through (a) a T2 weighted MRI and (b) the corresponding image after bias-field correction, with arrows indicating regions that are particularly improved by the processing. The “closed” T2w image is shown in (c) and foreground mask I_{fg} in (d). In each image the top-left quadrant is the axial slice, the top-right is sagittal and the bottom-left is coronal.

- 243 5. Landmark identification. The most anterior voxels in the foreground mask, I_{fg} , on
 244 the left and right sides of the volume, are identified and assumed to be approximately
 245 coincident with the nipple locations. If multiple voxels are found then the center of
 246 mass of the cluster is computed. The mid-sternum is computed as the most anterior
 247 voxel of the foreground mask, equidistant from the nipple landmarks in the coronal
 248 plane.
- 249 6. Pectoral muscle boundary extraction. Various methods have been presented in the
 250 literature to segment breast MRI volumes and the pectoral muscle (Table I). These
 251 include semi-automated methods requiring user interaction^{31,33,36}, 2D mid-slice tem-
 252 plate registration³⁶, statistical shape models²⁵ and atlas-based methods^{16,18–20,24,45}.

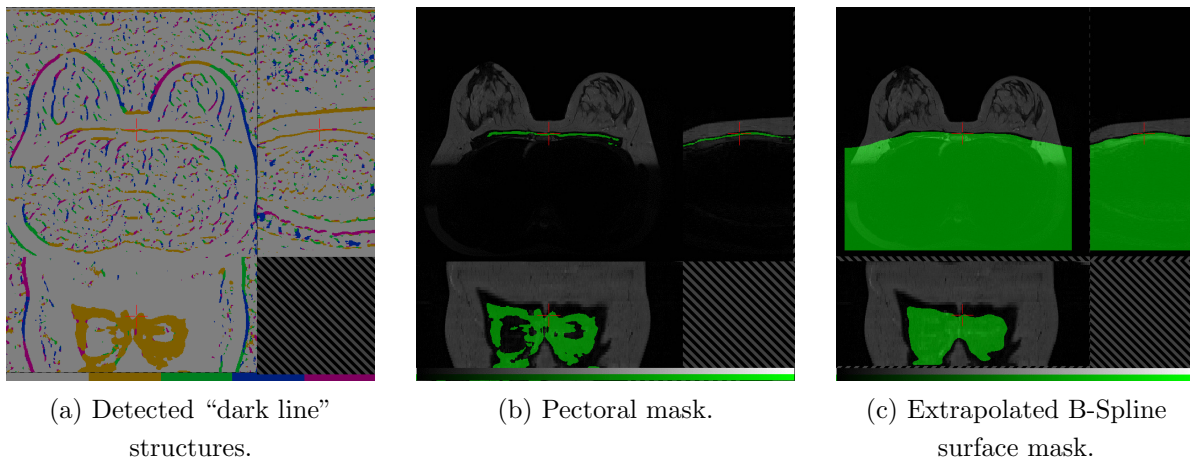


FIG. 3: The anterior pectoral muscle surface is detected using the Oriented Basic Image Feature “dark line” class. Subplot (a) shows these features detected at four orientations ($OBIF_{15}$ to $OBIF_{18}$). Region-growing the “brown” medial-lateral class, $OBIF_{15}$, closely delineates this anterior boundary immediately posterior to the sternum (b). The anterior surface of this mask is extrapolated using a B-Spline fit to the lateral boundaries of the volume (c).

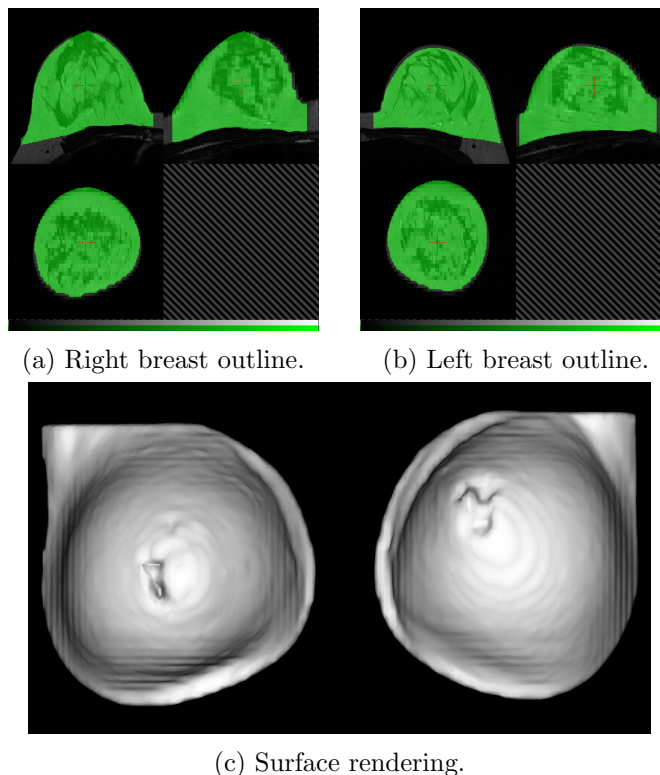


FIG. 4: Breast region mask created by removing the pectoral surface mask (figure 3c) from the foreground mask (figure 2d). Two views of the mask are shown, superimposed on the original MR image and centered on the right (a) and left (b) breasts. The surface rendering (c) illustrates the “squaring off” to include the axilla.

253 A number of methods have been developed to segment explicitly the pectoral mus-
 254 cle. These include a B-spline fit to the intensity gradient of the pectoral boundary³³,
 255 anisotropic diffusion and Canny edge detection¹⁷ and Hessian matrix planar shape
 256 filtering^{15,46}. Atlas-based methods have been shown to perform well but are compu-
 257 tationally intensive⁴⁷ and require significant initial investment of time to develop a
 258 library of atlases.

259 We have developed a method to detect explicitly the anterior pectoral muscle boundary
 260 in individual MR volumes. Our approach has similarities to the Hessian processing
 261 of Wang *et al.*^{15,46}, in that it employs Gaussian derivatives to detect regions in the
 262 image with a planar profile. However rather than computing a ratio of the eigenvalues
 263 of the Hessian matrix and thresholding the result, we obtain a direct classification of
 264 linear structures, immediately posterior to the sternum, using Oriented Basic Image
 265 Features (OBIFs, Figure 3).

266 The concept of Basic Image Features (BIFs) was developed by Griffin⁴⁸. The technique
 267 classifies pixels in a 2D image into one of seven classes according to the local zero-, first-
 268 or second-order structure. This structure is computed using a bank of six derivative
 269 of Gaussian filters (L_{00} , L_{10} , L_{01} , L_{20} , L_{11} and L_{02}) which calculate the nth (where
 270 $n=0,1,2$) order derivatives of the image in x and y (S_{00} , S_{10} , S_{01} , S_{20} , S_{11} and S_{02}).
 271 By combining the outputs of these filters, any given pixel can be classified according
 272 to the largest component of vector BIF:

$$\text{BIF} = \left\{ \begin{array}{l} \text{flat} \\ \epsilon S_{00}, 2\sqrt{S_{10}^2 + S_{01}^2}, \\ \text{slope-like} \\ \text{maximum} \quad \text{minimum} \\ \lambda \quad , \quad -\lambda \quad , \\ \text{light line} \quad \text{dark line} \\ \frac{\lambda + \gamma}{\sqrt{2}} \quad , \quad \frac{\lambda - \gamma}{\sqrt{2}} \quad , \quad \gamma \quad \text{saddle} \end{array} \right\} \quad (6)$$

273 given

$$\lambda = \sigma^2 \frac{(S_{20} + S_{02})}{2} \quad (7)$$

$$\gamma = \sigma^2 \sqrt{(S_{20} + S_{02})^2 + 4S_{11}^2} \quad (8)$$

$$(9)$$

274 In addition, slopes, light lines, dark lines and saddles can be characterised according to
 275 their orientation (OBIFs). We quantise this orientation into four, 45 degree quadrants
 276 which produces eight slope sub-classes (OBIF₁ to OBIF₈), and four sub-classes for
 277 each of light lines (OBIF₁₁ to OBIF₁₄), dark lines (OBIF₁₅ to OBIF₁₈) and saddles
 278 (OBIF₁₉ to OBIF₂₂).

279 By region-growing the medial-lateral, OBIF₁₅ dark line features detected in each axial
 280 image slice, in 3-D, from seed positions immediately posterior to the mid-sternum,
 281 we obtain a binary segmentation of the anterior pectoral muscle surface. The BIF
 282 processing was performed at a single scale using a Gaussian kernel with standard
 283 deviation 5 mm. A smooth B-spline surface is then fitted to the anterior voxels of
 284 the resulting mask⁴⁴ to extrapolate the muscle surface to the lateral boundaries of the
 285 image volume (figure 3c).

286 7. Finally we generate a 2D coronal mask, I_{CNL} , to crop non-breast tissue from the
 287 whole breast mask. I_{CNL} is computed from a coronal skin elevation map, I_{skin2D} ,
 288 which contains the distance of each anterior skin voxel in the foreground mask, I_{fg} ,
 289 from the most posterior boundary of the MR volume. The coronal profile of each
 290 breast is obtained by thresholding I_{skin2D} at

$$h = \frac{(4h_{ms} + h_{Ln} + h_{Rn})}{6} \quad (10)$$

291 where h_{ms} is the anterior elevation of the mid-sternum landmark, and h_{Ln} and h_{Rn} are
 292 the left and right nipple anterior elevations respectively. The roughly circular profile
 293 obtained for each breast is then dilated by 10mm and the mask squared off, to create
 294 a superior-lateral corner and hence extend the breast volume into the axilla (figure 4c)

295 **C. Fat-Water Discrimination**

296 **1. *Semi-automated calculation of percentage breast density, based on Dixon***
 297 ***Images***

298 In principle, the output from a Dixon pulse sequence is a set of images reflecting water
 299 content $I_w(\mathbf{r})$, which we identify with the parenchymal component of the breast, and an
 300 equivalent set $I_f(\mathbf{r})$ reflecting fat content. Ideally, these images would be quantitative and
 301 allow the direct calculation of the water and fat fractions $\phi_w(\mathbf{r})$ and $\phi_f(\mathbf{r})$ via the equation⁴⁹

$$\phi_w = \frac{I_w}{I_w + I_f} \quad \text{and} \quad \phi_f = \frac{I_f}{I_w + I_f} \quad (11)$$

302 In practice, there are a number of complicating factors:

- 303 • Parenchymal tissue and fat have different relaxation properties and, since the acqui-
 304 sitions are not generally designed to be proton density weighted, this means that the
 305 relative intensities of equal fractions of fat and water are different.
- 306 • The B_1 field of the probe is not uniform across the whole breast and this leads to a
 307 spatially-dependent efficacy of the fat-water separation.
- 308 • In practice, the fat tissue does not have a single proton resonance.
- 309 • Different manufacturers have different proprietary image reconstruction methods and
 310 these may influence the quantitative results.

311 Our solution to (at least) the first of these problems is to proceed as follows:

312 (a) Identify a small region in the water image that is expected to be entirely composed
 313 of parenchymal tissue. The region should be in a part of the image that is free from
 314 intensity artefacts caused by proximity to the RF coil (i.e., the data should come from
 315 a homogenous region of B_1).

316 (b) In the fat image, identify similarly a second region entirely composed of fat.

317 (c) Calculate the ratio of the average voxel values in each of the two regions:

$$r = \frac{1}{N_w} \sum_{i \in \text{ROI}_w} I_w(\mathbf{r}_i) \bigg/ \frac{1}{N_f} \sum_{j \in \text{ROI}_f} I_f(\mathbf{r}_j) \quad (12)$$

318 where N_w and N_f are the numbers of voxels in the selected regions-of-interest ROI_w and
 319 ROI_f respectively.

320 (d) Replace the value I_f in Eq. (11) with rI_f .

321 This procedure potentially improves the accuracy of the water-fraction calculation but at
 322 the cost of introducing an interactive step into the density estimation process. We have not
 323 tested in a systematic fashion the influence that the size and shape of the region-of-interest
 324 selection have on the process, in part because we have no ground truth values. A further
 325 issue with this technique is that in the limiting cases of extremely dense or extremely fatty
 326 tissues, it may not be possible to find appropriately “pure” regions of both types.

327 2. *Fully-automated, using T1w and T2w Images*

328 Fuzzy c-means (FCM) clustering has been evaluated by a number of studies to classify
 329 the internal structure of the breast into fat and fibro-glandular tissue classes^{16,18,29,31,33–35,50}
 330 Table I). Song *et al.*⁵⁰ adopt a Gaussian kernel FCM, whilst Sathya³⁴ use a quadratic kernel
 331 FCM to train a support vector machine (SVM). In²⁹, Wang *et al.* use a multi-parametric
 332 hierarchical SVM classification approach to segment the internal breast and found this to be
 333 superior to both a conventional SVM²⁸ and FCM segmentation. T1W, T2W, proton density
 334 and three point Dixon (water and fat) images were all incorporated. Klifa *et al.*³¹ compared
 335 the resulting volumetric MRI density measurement of their method with mammography
 336 but found only modest correlation ($R^2 = 0.67$).

337 In²⁰ a probabilistic atlas approach was proposed. This requires a sizeable number of
 338 pre-labelled atlases to be created, considerable computation to register them and assumes
 339 correspondence between fibro-glandular structures across the population. To address the
 340 latter a Markov Random Field (MRF) was introduced to spatially regularise the classification
 341 of each voxel according to that of its neighbours. Similarly Wu *et al.*¹⁶ use the registered atlas
 342 as a pixel-wise fibroglandular likelihood prior for a multivariate Gaussian mixture model and
 343 demonstrate superior performance when compared to FCM using a manual thresholding
 344 approach as the gold standard. In a later publication¹⁹, the same authors investigate a
 345 continuous max-flow (CMF) algorithm to generate a voxel-wise likelihood map using the
 346 same atlas initialisation. They demonstrate that this approach performs better with the

347 atlas initialisation than without, but that FCM is superior to the CMF approach without
348 the atlas.

349 Mixture models have also been proposed by Yang *et al.*³² who implement a method using
350 Kalman filter-based linear mixing. They demonstrate it out-performs a c-means method but
351 evaluation using real MR data was limited.

352 Our segmentation of the T1 and T2 MRI data into fat and glandular tissue is a mod-
353 ification of that proposed by Van Leemput *et al.*⁵¹ in which an intensity model and spa-
354 tial regularization scheme are optimized using a Maximum Likelihood formulation of the
355 Expectation-Maximisation (EM) algorithm. The EM algorithm iteratively updates the
356 Gaussian probability distributions used to estimate the intensity histograms of each tis-
357 sue class (fat and non-fat) via a Maximum Likelihood formulation. In order to improve
358 classification of voxels in which the partial volume of fat and glandular tissues is a signif-
359 icant factor, a Markov Random Field (MRF) regularization scheme is employed to ensure
360 spatial consistency. The MRF modifies the probability of a particular voxel being assigned
361 to either the fat or glandular classes (or a proportion of either) according to the current clas-
362 sification of neighbouring voxels. In this way isolated regions of glandular tissue in very fatty
363 regions, for instance, are penalized in favour of a more realistic and anatomically correct
364 arrangement of the classes.

365 D. Epidemiology

366 Appropriate linear and logistic regression models were used to examine associations of
367 average total breast, fat and water volumes, and percent water, as measured using different
368 MR images and segmentation methods, with selected established and potential mammo-
369 graphic density correlates. Breast measures were log-transformed and the exponentiated
370 estimated regression parameters represent the relative change (RC) in breast measure with
371 a unit increase, or category change, in the exposure of interest (with 95% confidence intervals
372 (95% CI) calculated by exponentiating the original 95% CIs). Age at menarche (months),
373 height (cm) and BMI (height (cm)/ weight (kg)²) at MR were treated as continuous vari-
374 ables and centred at the mean. Current hormone contraceptive use, cigarette smoking and
375 alcohol drinking were treated as binary (yes/no) variables. Mothers mammographic den-
376 sity (%) was averaged between both breasts, and maternal age (months) at mammography

377 and clinically measured or self-reported maternal BMI (median 3 years (inter-quartile range
 378 (IQR) = 1.5 years) prior to mammography)) were used as continuous measures and centred
 379 at the mean. Variables were included as potential determinants of breast measures, or as
 380 confounding factors, where appropriate.

381 Data analysis was conducted with STATA statistical software, Version 14.

382 III. RESULTS

383 A. Breast Outline Segmentation

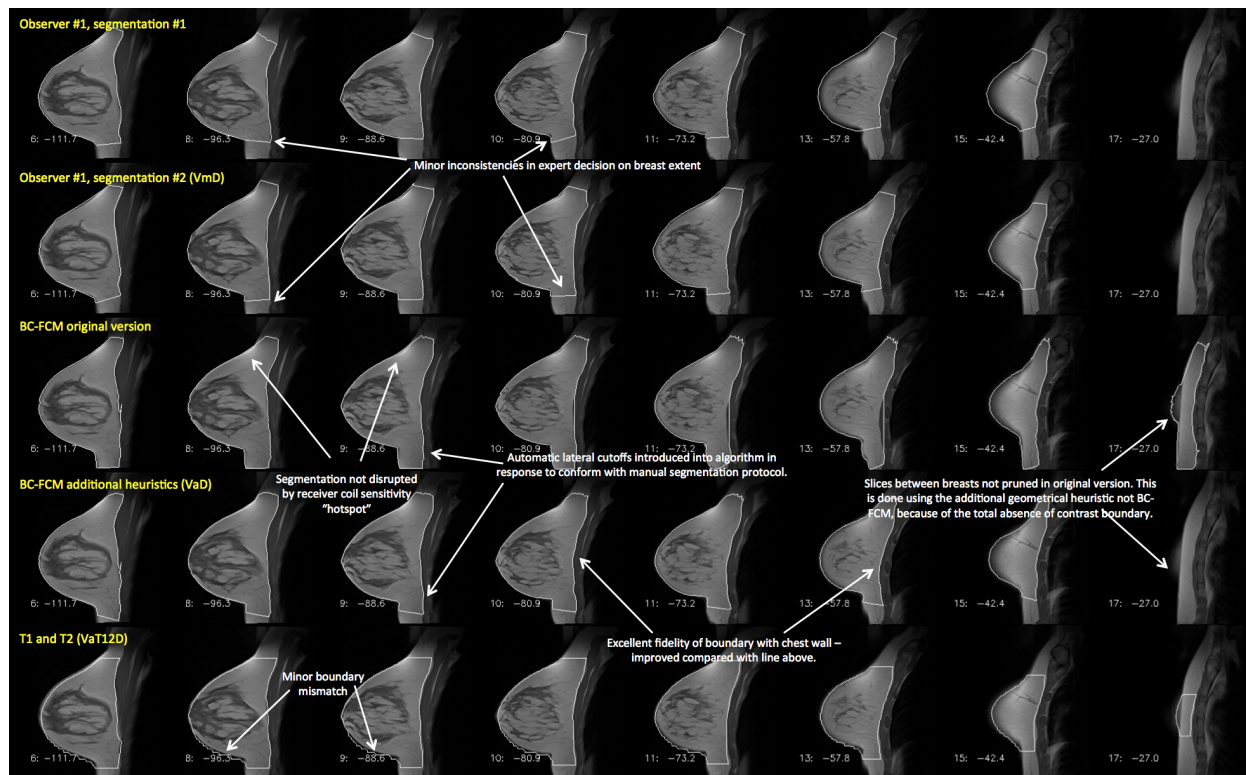


FIG. 5: : Example of a case where both of the algorithms examined in this work performed well. Features of interest in the various different segmentations are annotated. *Note that this image is provided with high resolution and can be zoomed significantly to reveal additional detail.*

384 Figure 5 shows an example of the two methods applied to a dataset containing medium-
 385 sized breasts, with a moderate parenchymal content. There is a border of fat around the
 386 parenchyma, which, at the posterior of the breast, leads to excellent contrast at the bound-
 387 ary with the chest wall, making segmentation a relatively straightforward task. Results are

TABLE II: : Dice and Jaccard coefficients for the “easy” segmentation problem of Fig. 5. Note that the BC-FCM/heuristics (VaD) represents the fully automated version, running with default parameters.

| | Manual 1 | Manual 2 | BC-FCM Orig | BC-FCM /heuristics (VaD) | VaT12D |
|-----------------------------|----------|----------|----------------|--------------------------------|--------|
| Dice Coefficients | | | | | |
| Manual 1 | 1.000 | | | | |
| Manual 2 | 0.949 | 1.000 | | | |
| BC-FCM Orig | 0.854 | 0.877 | 1.000 | | |
| BC-FCM/heuristics (VaD) | 0.901 | 0.924 | 0.921 | 1.000 | |
| VaT12D | 0.887 | 0.888 | 0.810 | 0.865 | 1.000 |
| Jaccard Coefficients | | | | | |
| Manual 1 | 1.000 | | | | |
| Manual 2 | 0.904 | 1.000 | | | |
| BC-FCM Orig | 0.745 | 0.781 | 1.000 | | |
| BC-FCM/heuristics | 0.820 | 0.859 | 0.853 | 1.000 | |
| VaT12D | 0.797 | 0.799 | 0.681 | 0.761 | 1.000 |

388 shown for two separate manual segmentations by the same experienced observer; for the
389 BC-FCM method from ref.³⁷; the BC-FCM method with additional heuristics and default
390 parameters, as described above; and the new method based on T1 and T2 images (VaT12).
391 It will be seen that the segmentation performance is excellent, with only minor difference
392 between the methods. Note how implementation of guidelines developed during the manual
393 segmentation process supplements the BC-FCM approach in order to cut off the segmenta-
394 tion in both the left-right and superior-inferior directions, where there are no corresponding
395 intensity boundaries seen in the image data themselves.

396 Table II shows the Dice and Jaccard coefficients for the four sets of segmentations illus-
397 trated in Figure 5, confirming the excellent performance of all the algorithms.

398 By contrast, Figure 6 illustrates a case where all assessment methods have far more
399 difficulty in providing a correct segmentation. Smaller breasts tend to be more problematic
400 to segment, as a higher fraction of the segmentation involves partial-volume effects. Highly
401 parenchymal breasts have very low (sometimes no) contrast between the parenchyma and
402 pectoral muscles of the chest wall, and the intensity-based BC-FCM algorithm has particular
403 difficulties in this regard. Many slices require a high degree of anatomical knowledge to
404 perform the segmentation. Consider the two versions of the BC-FCM results presented.
405 With the default parameters in the upper of the two rows, over-segmentation occurs in slice

TABLE III: : Dice and Jaccard coefficients for the difficult segmentation problem of Fig. 6

| | Manual 1 | Manual 2 | BC-FCM Orig | BC-FCM /heuristics (best) | BC-FCM Edited (VsD) | VaT12D |
|-----------------------------|----------|----------|----------------|---------------------------------|---------------------------|--------|
| Dice Coefficients | | | | | | |
| Manual 1 | 1.000 | | | | | |
| Manual 2 | 0.915 | 1.000 | | | | |
| BC-FCM Orig | 0.776 | 0.797 | 1.000 | | | |
| BC-FCM /heuristics (best) | 0.836 | 0.792 | 0.782 | 1.000 | | |
| BC-FCM Edited (VsD) | 0.914 | 0.913 | 0.809 | 0.828 | 1.000 | |
| VaT12D | 0.796 | 0.771 | 0.728 | 0.818 | 0.795 | 1.000 |
| Jaccard Coefficients | | | | | | |
| Manual 1 | 1.000 | | | | | |
| Manual 2 | 0.843 | 1.000 | | | | |
| BC-FCM Orig | 0.634 | 0.662 | 1.000 | | | |
| BC-FCM /heuristics (best) | 0.718 | 0.657 | 0.642 | 1.000 | | |
| BC-FCM Edited (VsD) | 0.842 | 0.840 | 0.679 | 0.707 | 1.000 | |
| VaT12D | 0.661 | 0.627 | 0.572 | 0.692 | 0.660 | 1.000 |

406 11 and part of the chest wall is included in the parenchymal breast region. By contrast, with
407 the “best” set of parameters (as found by repeating the algorithm and manually adjusting
408 them), the lower row shows that the problem in slice 11 is corrected, with good matching of
409 the pectoral muscle contour, but only at the cost of introducing an under-segmentation in
410 slice 8, and, worse, losing the segmented breast region entirely in slice 6. In practice, where
411 such problems occurred, it was necessary to edit the final segmentations manually. (Note on
412 terminology: As shown in Fig. 6, the “BC-FCM/heuristics (VaD)” method cannot reliably
413 be run for the whole cohort using only default parameters and so we must describe the
414 technique as semi- rather than fully-automated. Even for cases where no manual editing or
415 parameter adjustment need to be performed, human inspection is still required to confirm
416 this. All subsequent cohort statistics will therefore use the nomenclature VsD to reflect
417 this.)

418 We have run a similar analysis on all 16 cases for which we have duplicate manual
419 segmentations by all three observers. The detailed results are shown in the Supplementary
420 Information.

421 A second method of examining the relation between the volume segmentation results is
422 to plot the total breast volume obtained by one method against that of another. In the

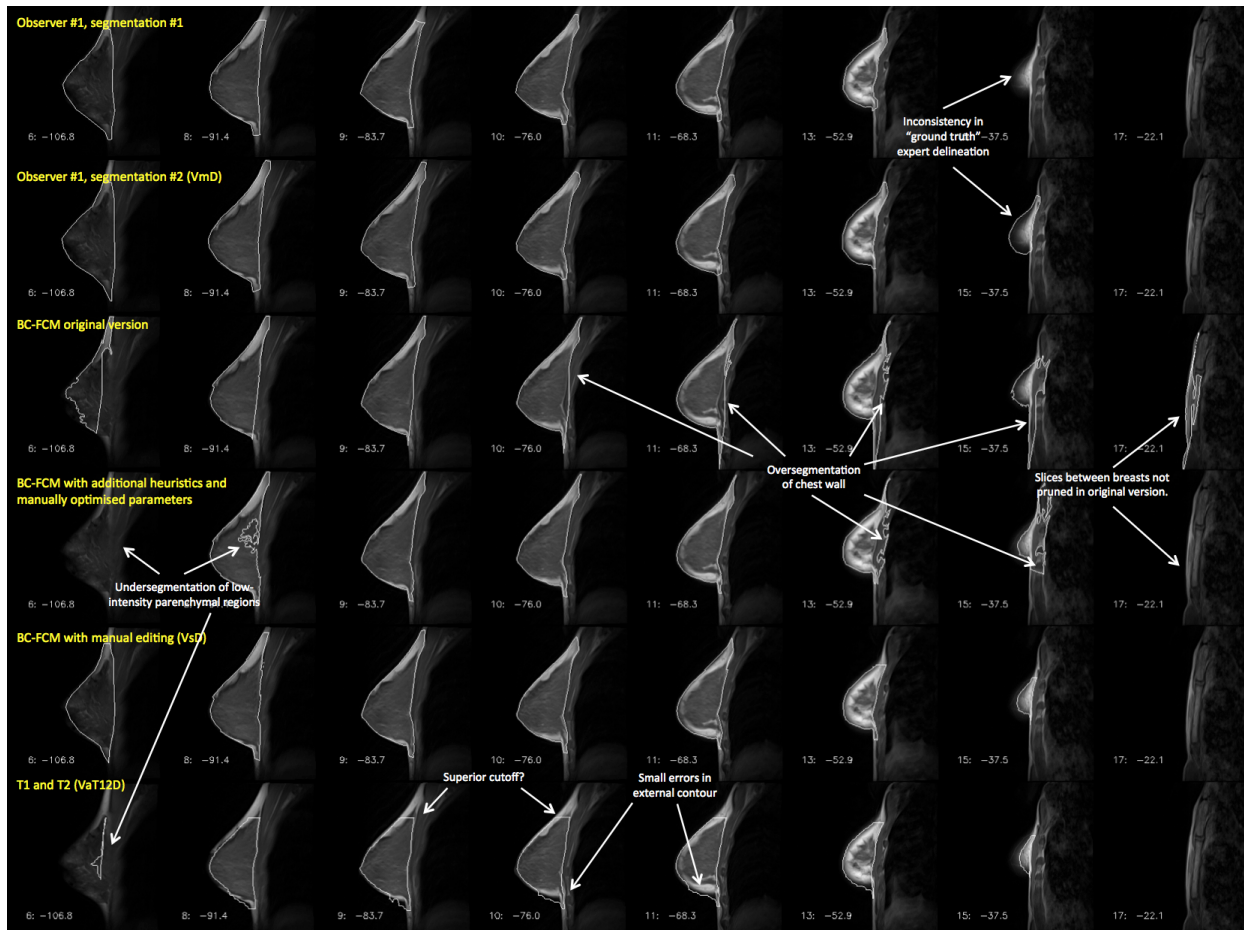


FIG. 6: : Example of a case where automatic segmentation is difficult. The rows represent the results of different segmentations and, for compactness, an informative subset of slices has been chosen to illustrate important features of the problem. *Note that this image is provided with high resolution and can be zoomed significantly to reveal additional detail.*

423 scatter plots of Figures 7(a)–(c), the x - and y -coordinates of each point represent the mean,
 424 for a single subject, of the left and right breast volumes evaluated, respectively, by the two
 425 methods under consideration. Figure 7(a) compares VsD, the semi-automated BC-FCM
 426 method using Dixon image input, with the “gold-standard” median manual segmentation,
 427 VmD, measured on the same Dixon dataset. Figure 7(b) gives results for the VaT12 method,
 428 which operates on the T1w and T2w datasets and evaluates the breast volume in the coordi-
 429 nate space of the T1w dataset. Finally, Figure 7(c) looks at the effect of resampling the
 430 map generated by the algorithm in (b) with the spatial resolution and frame of reference of
 431 the Dixon data, which we term VaT12D. In each case, the line of identity is shown and Ta-
 432 ble IV reports the corresponding inter-class correlations (ICC), representing the proportion
 433 of variance across participants shared between different ascertainment methods.

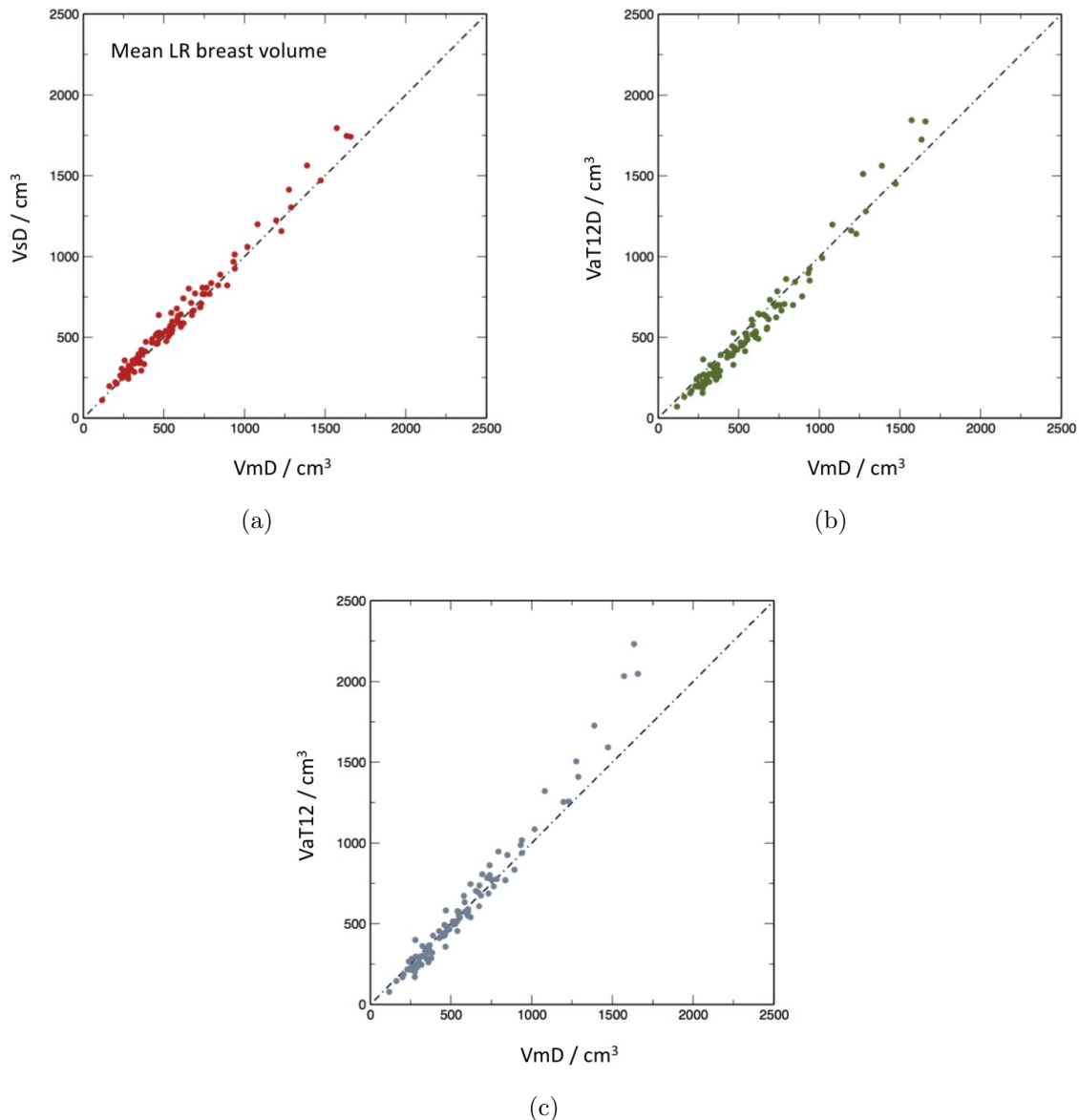


FIG. 7: Scatter plots of mean left and right breast volumes in cm³ for the different methods in comparison to manual segmentation: (a) volume from semiautomatic segmentation of Dixon images (VsD) vs volume from manual segmentation (VmD); (b) volume via automated segmentation from T₁- and T₂-weighted images transformed to Dixon reference frame (VaT12FD) vs manual (VmD); (c) volume obtained from T₁- and T₂-weighted images in native 3-D reference frame (VaT12).

TABLE IV: : Inter-class correlations for total breast volume segmentations.

| | VmD | VsD | VaT12D | VaT12 |
|--------|-------|-------|--------|-------|
| VmD | 1.000 | | | |
| VsD | 0.990 | 1.000 | | |
| VaT12D | 0.974 | 0.977 | 1.000 | |
| VaT12 | 0.985 | 0.992 | 0.982 | 1.000 |

TABLE V: : Inter-class correlations for total water volume segmentations.

| | VmD-FWsD | VsD-FWsD | VaT12D-FWsD | VaT12-FWaT1 | VaT12-FWaT2 |
|-------------|----------|----------|-------------|-------------|-------------|
| VmD-FWsD | 1.000 | | | | |
| VsD-FWsD | 0.995 | 1.000 | | | |
| VaT12D-FWsD | 0.992 | 0.993 | 1.000 | | |
| VaT12-FWaT1 | 0.920 | 0.921 | 0.924 | 1.000 | |
| VaT12-FWaT2 | 0.948 | 0.949 | 0.962 | 0.899 | 1.000 |

434 B. Fat-Water Segmentation

435 Figures 8 and 9 present the results of the fat and water segmentation in the same format
 436 as for the total breast volume. In this case, however, a further option is available. Although
 437 the breast outline segmentation VaT12 requires both the T1w and T2w data, once this
 438 mask is available, it is possible to obtain two separate fat-water segmentations one using
 439 just the T1w and one using just the T2w data. These are denoted VaT12-FWaT1 and
 440 VaT12-FWaT2 respectively.

441 The inter-class correlation (ICC) for total water volume, representing the proportion of
 442 variance across participants shared between the different ascertainment methods, are given
 443 in table V.

444 C. Epidemiological Results

445 A diagrammatic summary of the results of the epidemiological analysis is presented in
 446 Figure 10 and further details of the work are reported as supplementary information.

447 Associations with both breast volume and breast water fraction were found for current
 448 body mass index (BMI). For a 1 kg m⁻² increase in BMI, a relative change in breast volume
 449 of 1.13[1.10, 1.16] was observed for the cohort for both the VmD and VsD methods and
 450 the corresponding result for the VaT12 family of methods was 1.15[1.12, 1.18], where the
 451 figures in square brackets are the 95% confidence intervals. A smaller, but still important,
 452 decrease in breast water fraction was seen, and the corresponding statistics are VmD-FWsD,
 453 VsD-FWsD 0.96[0.95, 0.97], VaT12D-FWsD 0.95[0.94, 0.97], VaT12-FWaT1 0.97[0.96, 0.98],
 454 VaT12-FWaT2 0.95[0.94, 0.96].

455 A weak association between current height and breast volume was also observed. For

456 a 1 cm increase in height, the analysis methods gave the following relative increases in
 457 breast volume: VmD 1.05[0.98, 1.11], VsD 1.04[0.98,1.11], VaT12D-FWsD was 1.05[0.97,
 458 1.12], VaT12-FWaT1 1.05[0.95, 1.03], VaT12-FWT2 1.05[0.95, 1.13]. However, height was
 459 not associated with breast water fraction.

460 No associations were found with any of: age of menarche, use of oral contraception,
 461 smoking, alcohol intake or maternal mammographic density.

462 From the similarity of all these statistics, we conclude that the exact details of the seg-
 463 mentation methods are not significant at the level of this cohort analysis.

464 IV. DISCUSSION

465 Our results show that, as in many segmentation problems, the degree of success of the au-
 466 tomated algorithms varies significantly between subjects. Figure 5 and Table II demonstrate
 467 excellent performance by all of the algorithms, whereas the degree of correspondence with
 468 the expert manual segmentation is considerably poorer in Figure 6 and Table III. However,
 469 it should be noted that even the expert human observer is less able to provide a good repeat
 470 segmentation.

471 The ICCs for total breast volume in Table IV demonstrate good agreement between
 472 all methods, but interestingly, slightly closer agreement between VaT12 and the two Dixon-
 473 based methods (VmD or VsD) than between VaT12D and the Dixon methods. As described
 474 above, VaT12D is created by simply resampling VaT12 in the Dixon coordinate space, which
 475 has a coarser slice thickness, using appropriate blurring and nearest neighbour interpolation.
 476 Although movement between the Dixon and T1w or T2w scans could explain this disparity,
 477 registering the volumes did not improve the results. The resampling process appears to
 478 amplify the difference between VaT12 and VmD or VsD, but we have not analysed this
 479 further, given that it is a relatively small effect.

480 It would, of course, be interesting to compare the output of the VaT1T2 method di-
 481 rectly with manual segmentation of the high-resolution T1w dataset in its native refer-
 482 ence frame, without the need to down-sample. However, the workload involved in creating
 483 high-resolution manual segmentations is prohibitive. In the Supplementary Information, we
 484 report anecdotal results for five such cases with full high-resolution manual segmentations.

485 Also of note from comparison of the scatter-plots of Figure 7 is that each of methods VsD,

486 VaT12D and VaT12 increasingly over-estimates the breast volume in comparison to VmD as
 487 the mean left and right breast size increases. This is most apparent for VaT12. The trend to
 488 larger error is, of course logical – similar percentage errors between the methods will result
 489 in greater absolute differences the larger the breast – but it is not currently clear why all
 490 methods are biased to *over*-estimate the volume in this region. Method VaT12D also *under*-
 491 estimates the breast volume for smaller breasts compared with the manual segmentation
 492 VmD and the reason for this, too, is unclear.

493 The biggest discrepancy between analysis methods, as shown by the scatter plots, is in the
 494 assessment of mean breast water volume (and, hence, water fraction — data not shown). The
 495 VsD-FWsD and VaT12-FWsD methods both use Dixon source data and differ from VmD-
 496 FWsD only via the breast outline previously described. The methods all give very similar
 497 results (ICCs 0.995 and 0.992 in Table V). By contrast, the correlation between the Dixon-
 498 based VmD-FWsD and VaT12-FWaT1 is weaker, and the VaT12-FWaT2 result additionally
 499 shows a bias (Figure 8). However, it is important to note that the assumption that water
 500 fractions based on the Dixon method can be regarded as a gold standard for true parenchymal
 501 fraction is much less compelling than the previous assumption that VmD is the gold-standard
 502 volume. We justify our choice of VmD-FWsD as the method of comparison on the basis that
 503 it is consistent with previous work in the field⁴⁹ (and indeed an improvement), but Ledger
 504 *et al.*⁵² have demonstrated that there is a significant degree of variability between different
 505 Dixon-based methods, depending on the exact design of the pulse sequence. It is unsurprising
 506 that a segmentation based on a completely different MRI contrast mechanism should be less
 507 highly correlated. What is nevertheless highly encouraging is that the correlation remains
 508 as strong as it is — the worst value reported in Table V is 0.920 — and this suggests that
 509 the use of MRI as a modality will prove to be a robust choice for breast analysis.

510 A salutary lesson from the scatter graphs is the constant need for vigilance and appropri-
 511 ate quality control when processing large cohorts of data. During the review of this paper a
 512 referee noticed an outlier, which turned out to be the result of an easily-corrected error that
 513 caused the mask for the entire right breast to be missing. Such “edge” cases, occurring very
 514 infrequently, remain a significant challenge in the adoption of automated pipelines. Any
 515 requirement for manual inspection of each dataset to check the output negates to some ex-
 516 tent the advantages of fully-automated segmentation processes, and an appropriate balance
 517 needs to be determined for each application.

518 Another feature highlighted by all of these results is the problem inherent in the use of
519 quantitative metrics such as Dice and correlation coefficients, which (despite their apparent
520 calculation “accuracy”) are a very blunt tool for analysing a complex situation. Are all of
521 the voxels that fail to overlap equally important? Is much of the difference between the
522 observer and the automated methods in fact caused by the choice of how much of the axilla
523 is included and is this region of any significance biologically?

524 A first reading of the coefficients presented here suggests that the VsD breast outline
525 segmentation, followed by the FWsD tissue segmentation method is the best-performing of
526 the computer-aided tools presented here. But is it the most suitable? Ultimately, the choice
527 of segmentation method needs to weigh up the following points:

- 528 • To what extent does the application demand a segmentation that is as good as that
529 of an expert radiologist? Two extremes here might be the planning of radiotherapy
530 treatment for an individual patient, where high correspondence is vital, and the cal-
531 culation of epidemiological parameters for a Big Data cohort, where errors might well
532 “average out.”
- 533 • To what extent is the ground truth knowable? For a given set of intra- and inter-
534 observer performance metrics evaluated on a test cohort, what performance thresholds
535 should be regarded as “acceptable” for automated segmentations?
- 536 • How widely available are the required source data? As previously noted, the Dixon
537 protocol is not routinely included in clinical examinations, thus limiting the applica-
538 bility of breast density measurements based on the VsD-FWsD method.
- 539 • How robust is the method?
- 540 • To what extent are speed, convenience and consistency of method to be preferred over
541 accuracy?

542 In our case, consideration of all of the above led to the use of the VaT12 method, rather
543 than VsD, for segmentation of the remaining 300 cases in the cohort (results not presented).
544 This choice was made largely on the basis of improved automation and on the epidemiological
545 evidence from the 200-strong training and test datasets, as described in Section III C, where
546 key epidemiological parameters were found to be identical, within confidence limits, for both
547 methods.

548 **V. CONCLUSION**

549 We have presented what we believe to be the first detailed comparison on a large,
550 population-based cohort of two methods of breast-outline segmentation based on completely
551 different approaches. These have been coupled with two methods of fat-water discrimination
552 based on fundamentally different MR contrast mechanisms. All combinations of the meth-
553 ods studied are in very strong agreement, as seen both visually and via inter-class correlation
554 coefficients, and are suitable for large-scale epidemiological analysis. We have discussed the
555 assumptions behind the methods and posed a number of general questions that we believe
556 need to be answered each time a decision is made on whether and how to perform automated
557 segmentation.

558 **ACKNOWLEDGMENTS**

559 We are extremely grateful to all the families who took part in the ALSPAC study, the
560 midwives for their help in recruiting them, and the whole ALSPAC team, which includes
561 interviewers, computer and laboratory technicians, clerical workers, research scientists, vol-
562 unteers, managers, receptionists and nurses. In particular we would like to thank study
563 nurses, Elizabeth Folkes and Sally Pearce, and CRIC radiographer, Aileen Wilson, for per-
564 forming MRI acquisitions of all the participants. The UK Medical Research Council and
565 the Wellcome Trust (Grant ref: 102215/2/13/2) and the University of Bristol provide core
566 support for ALSPAC.

567 Authors SJD and MOL acknowledge CRUK and EPSRC support to the Cancer Imaging
568 Centre at ICR and RMH in association with MRC and Department of Health C1060/A10334,
569 C1060/A16464 and NHS funding to the NIHR Biomedical Research Centre and the Clinical
570 Research Facility in Imaging. Authors JH, BE and DH were funded by the European
571 7th Framework Program grants VPH-PRISM (FP7-ICT-2011-9, 601040), VPH-PICTURE
572 (FP7-ICT-2011-9, 600948) and the Engineering and Physical Sciences Research Council
573 grant MIMIC (EP/K020439/1). IdSS was supported by funding from Cancer Research UK
574 (grant number C405/A12730).

575 **DISCLOSURE**

576 The authors are not aware of any conflicts of interest.

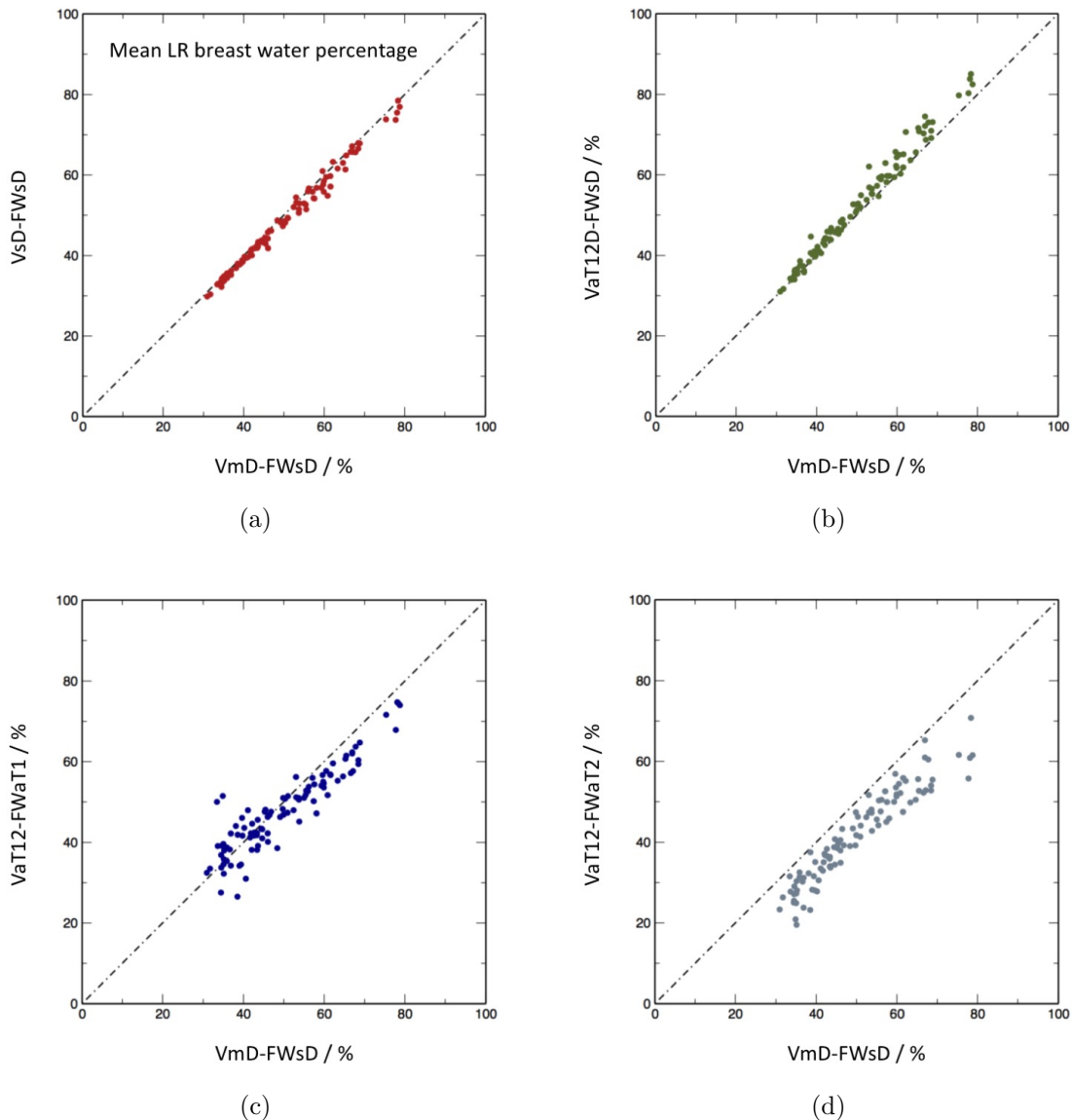


FIG. 8: Scatter plots of mean left and right breast water percentage for the different methods in comparison with manual segmentation on Dixon images followed by percentage water estimation the using semiautomated Dixon image method: (a) semiautomatic segmentation of Dixon images followed by percentage estimate from Dixon image data ($V_{sD}\text{-FWsD}$); (b) volume via automated segmentation from T_1 - and T_2 -weighted images transformed to Dixon reference frame (V_{aT12FD}) followed by semiautomated percentage estimate from the Dixon data ($V_{aT12D}\text{-FWsD}$); (c) volume obtained from T_1 - and T_2 -weighted images in native 3-D reference frame, followed by automatic percentage estimate from T_1 -weighted data ($V_{aT12}\text{-FWaT1}$); (d) as (c), but with the water percentage estimated from the T_2 -weighted data.

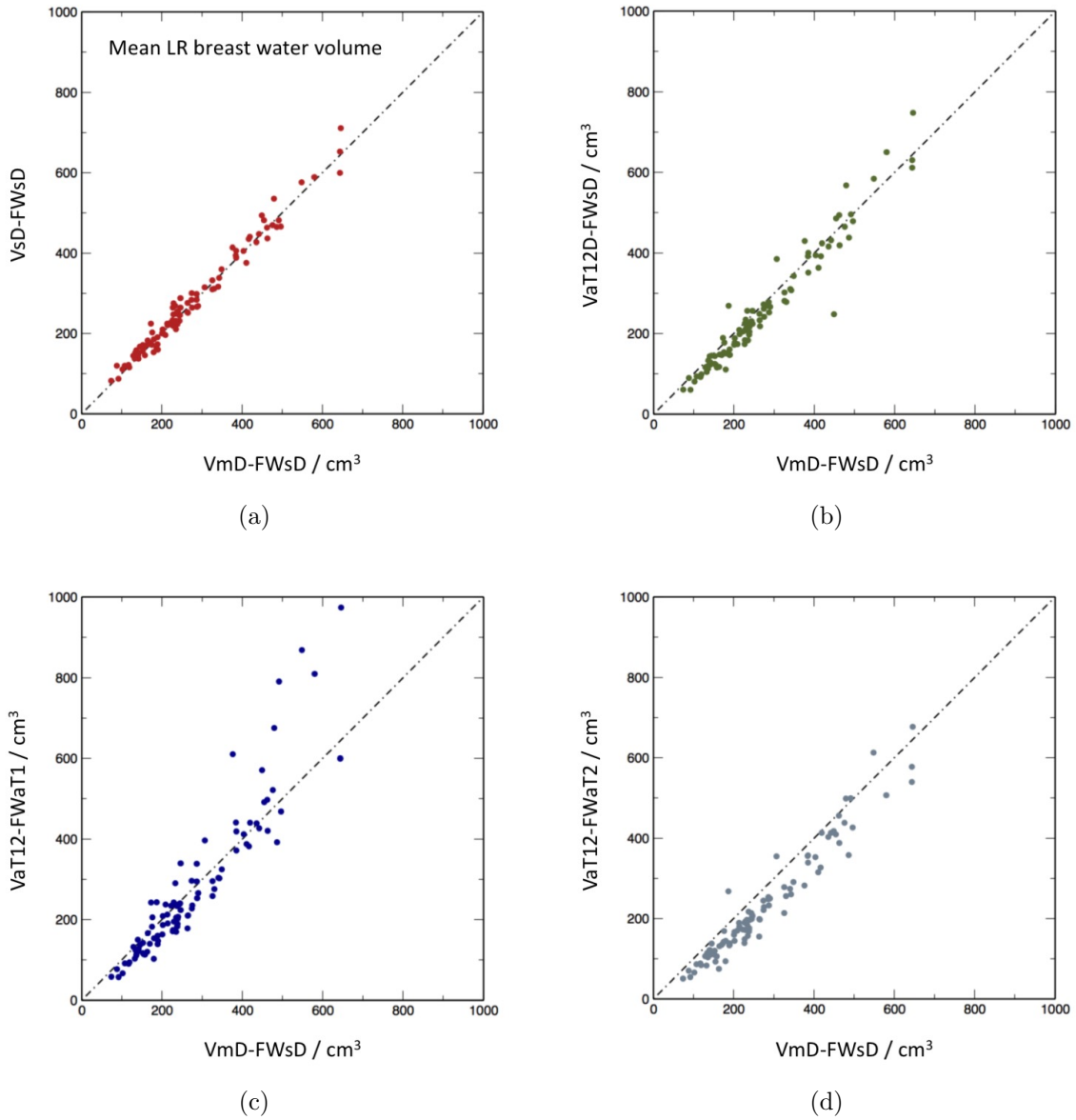


FIG. 9: Scatter plots of mean left and right breast water volumes in cm^3 for the different methods in comparison to $VmD-FWsD$. For nomenclature see caption to Figure 8.

Breast MRI segmentation for density estimation

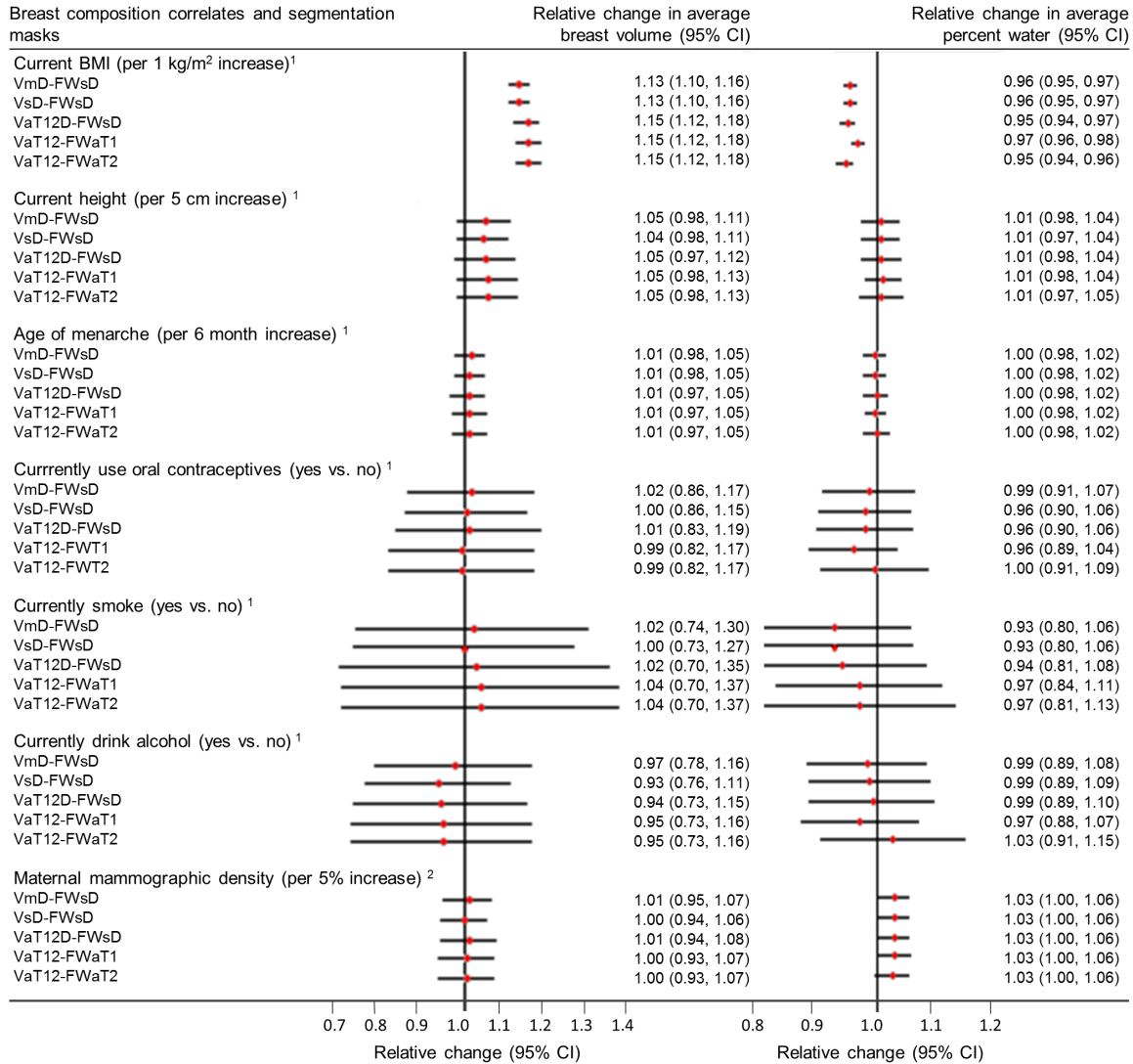


FIG. 10: Results of epidemiological analysis. Relative change in geometric means of MR breast volume and percent water in relation to a unit increase, or category change, in each breast composition correlate variable. ¹Models adjusted for current age in months and BMI at MR scan, where appropriate. ²Models restricted to young women for whom mammograms from their mothers could be retrieved (n=33) adjusted for current age in months and BMI at MR scan and maternal age at mammogram and BMI in 2010 (median=3y (IQR = 1.5y) prior to mammogram). For further details, see Supplementary Information.

577 **REFERENCES**

- 578 ¹V. A. McCormack and I. D. S. Silva, “Breast density and parenchymal patterns as markers
579 of breast cancer risk: A meta-analysis,” *Cancer Epidemiology Biomarkers & Prevention*
580 **15**, 1159–1169 (2006).
- 581 ²E. Vilapriño, C. Forne, M. Carles, M. Sala, R. Pla, X. Castells, L. Domingo, M. Rue,
582 and I. S. G. Interval Canc, “Cost-effectiveness and harm-benefit analyses of risk-based
583 screening strategies for breast cancer,” *Plos One* **9** (2014), 10.1371/journal.pone.0086858.
- 584 ³E. R. Price, A. W. Keedy, R. Gidwaney, E. A. Sickles, and B. N. Joe, “The potential impact
585 of risk-based screening mammography in women 40-49 years old,” *American Journal of*
586 *Roentgenology* **205**, 1360–1364 (2015).
- 587 ⁴S. Ciatto, N. Houssami, A. Apruzzese, E. Bassetti, B. Brancato, F. Carozzi, S. Catarzi,
588 M. P. Lamberini, G. Marcelli, R. Pellizzoni, B. Pesce, G. Risso, F. Russo, and A. Scorsolini,
589 “Categorizing breast mammographic density: intra- and interobserver reproducibility of
590 bi-rads density categories,” *Breast* **14**, 269–275 (2005).
- 591 ⁵R. Highnam, S. M. Brady, M. J. Yaffe, N. Karssemeijer, and J. Harvey, “Robust breast
592 composition measurement - volparatm,” in *Digital Mammography: 10th International*
593 *Workshop, IWDM 2010, Girona, Catalonia, Spain, June 16-18, 2010. Proceedings*, edited
594 by J. Mart, A. Oliver, J. Freixenet, and R. Mart (Springer Berlin Heidelberg, Berlin,
595 Heidelberg, 2010) pp. 342–349.
- 596 ⁶G. Waade, R. Highnam, I. Hauge, M. McEntee, S. Hofvind, E. Denton, J. Kelly, J. Sarwar,
597 and P. Hogg, “Error in recorded compressed breast thickness measurement impacts on
598 volumetric density classification using volpara v1.5.0 software,” *Medical Physics* **In press**
599 (2016).
- 600 ⁷A. Gubern-Mérida, M. Kallenberg, B. Platel, R. M. Mann, R. Mart, and N. Karssemeijer,
601 “Volumetric breast density estimation from full-field digital mammograms: A validation
602 study,” *PLoS ONE* **9**, e85952 (2014).
- 603 ⁸D. J. Thompson, M. O. Leach, G. Kwan-Lim, S. A. Gayther, S. J. Ramus, I. Warsi,
604 F. Lennard, M. Khazen, E. Bryant, S. Reed, *et al.*, “Assessing the usefulness of a novel
605 mri-based breast density estimation algorithm in a cohort of women at high genetic risk
606 of breast cancer: the uk maribs study,” *Breast Cancer Research* **11**, R80 (2009).
- 607 ⁹P. Hayton, P. Hayton, J. M. Brady, J. M. Brady, L. Tarassenko, L. Tarassenko, N. Moore,

- 608 and N. Moore, “Analysis of dynamic mr breast images using a model of contrast enhance-
609 ment,” *Medical Image Analysis* **1**, 207–24 (1997).
- 610 ¹⁰T. Twellmann, O. Lichte, and T. W. Nattkemper, “An adaptive tissue characterization
611 network for model-free visualization of dynamic contrast-enhanced magnetic resonance
612 image data,” *Medical Imaging, IEEE Transactions on* **24**, 1256–1266 (2005).
- 613 ¹¹M. Koenig, “Automatic cropping of breast regions for registration in mr mammography,”
614 *Proceedings of SPIE* **5747**, 1563–1570 (2005).
- 615 ¹²J. Yao, “Classification and calculation of breast fibroglandular tissue volume on spgr fat
616 suppressed mri,” *Proceedings of SPIE* **5747**, 1942–1949 (2005).
- 617 ¹³W. L. W. Lu, J. Y. J. Yao, C. L. C. Lu, S. Prindiville, and C. Chow, “Dce-mri segmentation
618 and motion correction based on active contour model and forward mapping,” *Seventh ACIS
619 International Conference on Software Engineering, Artificial Intelligence, Networking, and
620 Parallel/Distributed Computing (SNPD’06)*, 0–4 (2006).
- 621 ¹⁴V. Giannini, A. Vignati, L. Morra, D. Persano, D. Brizzi, L. Carbonaro, A. Bert, F. Sar-
622 danelli, and D. Regge, “A fully automatic algorithm for segmentation of the breasts in
623 dce-mr images,” in *Engineering in Medicine and Biology Society (EMBC), 2010 Annual
624 International Conference of the IEEE (IEEE)* pp. 3146–3149.
- 625 ¹⁵L. Wang, B. Platel, T. Ivanovskaya, M. Harz, H. K. Hahn, and Ieee, “Fully auto-
626 matic breast segmentation in 3d breast mri,” *2012 9th IEEE International Symposium
627 on Biomedical Imaging (ISBI)*, 1024–1027 (2012).
- 628 ¹⁶S. Wu, S. Weinstein, and D. Kontos, “Atlas-based probabilistic fibroglandular tissue
629 segmentation in breast mri,” *Medical image computing and computer-assisted interven-
630 tion : MICCAI ... International Conference on Medical Image Computing and Computer-
631 Assisted Intervention* **15**, 437–45 (2012).
- 632 ¹⁷S. Wu, S. P. Weinstein, E. F. Conant, A. R. Localio, M. D. Schnall, and D. Kontos, “Fully
633 automated chest wall line segmentation in breast mri by using context information,” in
634 *Medical Imaging 2012: Computer-Aided Diagnosis*, *Proceedings of SPIE*, Vol. 8315, edited
635 by B. VanGinneken and C. L. Novak (2012).
- 636 ¹⁸S. Wu, S. P. Weinstein, E. F. Conant, and D. Kontos, “Automated fibroglandular tissue
637 segmentation and volumetric density estimation in breast mri using an atlas-aided fuzzy
638 c-means method,” *Medical Physics* **40** (2013).
- 639 ¹⁹S. Wu, S. P. Weinstein, E. F. Conant, and D. Kontos, “Fully-automated fibroglandular

- 640 tissue segmentation and volumetric density estimation in breast mri by integrating a con-
 641 tinuous max-flow model and a likelihood atlas,” in *Medical Imaging 2013: Computer-Aided*
 642 *Diagnosis*, Proceedings of SPIE, Vol. 8670, edited by C. L. Novak and S. Aylward (2013).
- 643 ²⁰A. Gubern-Merida, M. Kallenberg, R. Marti, and N. Karssemeijer, “Multi-class proba-
 644 bilistic atlas-based segmentation method in breast mri,” in *Pattern Recognition and Image*
 645 *Analysis: 5th Iberian Conference, Ibpria 2011*, Lecture Notes in Computer Science, Vol.
 646 6669, edited by J. Vitria, J. M. Sanches, and M. Hernandez (2011) pp. 660–667.
- 647 ²¹A. Gubern-Mérida, M. Kallenberg, R. Mart, and N. Karssemeijer, “Segmentation of the
 648 pectoral muscle in breast mri using atlas-based approaches,” in *Medical Image Computing*
 649 *and Computer-Assisted Intervention MICCAI 2012* (Springer, 2012) pp. 371–378.
- 650 ²²A. Gubern-Mérida, M. Kallenberg, R. Mann, R. Marti, and N. Karssemeijer, “Breast
 651 segmentation and density estimation in breast mri: A fully automatic framework,” *IEEE*
 652 *Journal of Biomedical and Health Informatics* **19**, 349–357 (2015).
- 653 ²³C. Gallego-Ortiz and A. Martel, “Automatic atlas-based segmentation of the breast in mri
 654 for 3d breast volume computation,” *Medical physics* **39**, 5835–5848 (2012).
- 655 ²⁴F. Khalvati, C. Gallego-Ortiz, S. Balasingham, and A. L. Martel, “Automated segmen-
 656 tation of breast in 3-d mr images using a robust atlas,” *IEEE Transactions on Medical*
 657 *Imaging* **34**, 116–125 (2015), 0.
- 658 ²⁵C. Gallego and A. L. Martel, “Automatic model-based 3d segmentation of the breast in
 659 mri,” in *Conference on Medical Imaging 2011 - Image Processing*, Proceedings of SPIE,
 660 Vol. 7962 (2011).
- 661 ²⁶G. Ertas, H. O. Gulcur, M. Tunaci, and M. Dursun, “k-means based segmentation of
 662 breast region on mr mammograms,” *Magnetic Resonance Materials in Physics, Biology*
 663 *and Medicine* **19**, 317 (2006).
- 664 ²⁷G. Ertas, H. O. Gulcur, M. Tunaci, O. Osman, and O. N. Ucan, “A preliminary study
 665 on computerized lesion localization in mr mammography using 3d nmitr maps, multilayer
 666 cellular neural networks, and fuzzy c-partitioning,” *Medical physics* **35**, 195–205 (2008).
- 667 ²⁸C.-M. Wang, X.-X. Mai, G.-C. Lin, and C.-T. Kuo, “Classification for breast mri using
 668 support vector machine,” *8th IEEE International Conference on Computer and Informa-*
 669 *tion Technology Workshops: Cit Workshops 2008*, Proceedings , 362–367 (2008).
- 670 ²⁹Y. Wang, G. Morrell, M. E. Heibrun, A. Payne, and D. L. Parker, “3d multi-parametric
 671 breast mri segmentation using hierarchical support vector machine with coil sensitivity

- 672 correction,” *Academic Radiology* **20**, 137–147 (2013).
- 673 ³⁰C. Klifa, J. Carballido-Gamio, L. Wilmes, A. Laprie, C. Lobo, E. DeMicco, M. Watkins,
674 J. Shepherd, J. Gibbs, and N. Hylton, “Quantification of breast tissue index from mr data
675 using fuzzy clustering,” in *Engineering in Medicine and Biology Society, 2004. IEMBS’04.*
676 *26th Annual International Conference of the IEEE*, Vol. 1 (IEEE) pp. 1667–1670.
- 677 ³¹C. Klifa, J. Carballido-Gamio, L. Wilmes, A. Laprie, J. Shepherd, J. Gibbs, B. Fan,
678 S. Noworolski, and N. Hylton, “Magnetic resonance imaging for secondary assessment of
679 breast density in a high-risk cohort,” *Magnetic Resonance Imaging* **28**, 8–15 (2010).
- 680 ³²S.-C. Yang, C.-M. Wang, H.-H. Hsu, P.-C. Chung, G.-C. Hsu, C.-J. Juan, and C.-S. Lo,
681 “Contrast enhancement and tissues classification of breast mri using kalman filter-based
682 linear mixing method,” *Computerized Medical Imaging and Graphics* **33**, 187–196 (2009).
- 683 ³³K. Nie, J.-H. Chen, S. Chan, M.-K. I. Chau, H. J. Yu, S. Bahri, T. Tseng, O. Nalcioglu,
684 and M.-Y. Su, “Development of a quantitative method for analysis of breast density based
685 on three-dimensional breast mri,” *Medical Physics* **35** (2008).
- 686 ³⁴A. Sathya, S. Senthil, and A. Samuel, “Segmentation of breast mri using effective fuzzy c-
687 means method based on support vector machine,” *Proceedings of the 2012 World Congress*
688 *on Information and Communication Technologies*, 67–72 (2012).
- 689 ³⁵M. Lin, S. Chan, J.-H. Chen, D. Chang, K. Nie, S.-T. Chen, C.-J. Lin, T.-C. Shih, O. Nal-
690 cioglu, and M.-Y. Su, “A new bias field correction method combining n3 and fcm for
691 improved segmentation of breast density on mri,” *Medical Physics* **38**, 5–14 (2011).
- 692 ³⁶M. Lin, J.-H. Chen, X. Wang, S. Chan, S. Chen, and M.-Y. Su, “Template-based automatic
693 breast segmentation on mri by excluding the chest region,” *Medical Physics* **40** (2013).
- 694 ³⁷G. Ertas, S. J. Doran, and M. O. Leach, “A computerized volumetric segmentation method
695 applicable to multicentre mri data to support computer aided breast tissue analysis, density
696 assessment and lesion localization,” *Medical and Biological Engineering and Computing*,
697 1–12 (2016).
- 698 ³⁸W. T. Dixon, “Simple proton spectroscopic imaging,” *Radiology* **153**, 189–194 (1984).
- 699 ³⁹P. H. England, “Breast screening: professional guidance,” (2016).
- 700 ⁴⁰A. Boyd, J. Golding, J. Macleod, D. A. Lawlor, A. Fraser, J. Henderson, L. Molloy,
701 A. Ness, S. Ring, and G. Davey Smith, “Cohort profile: the ‘children of the 90s’ – the
702 index offspring of the avon longitudinal study of parents and children.” *Int J Epidemiol*
703 **42**, 111–127 (2013).

- 704 ⁴¹<http://www.bris.ac.uk/alspac/researchers/data-access/data-dictionary>.
- 705 ⁴²D. L. Pham and J. L. Prince, “An adaptive fuzzy c-means algorithm for image segmen-
706 tion in the presence of intensity inhomogeneities,” *Pattern Recognition Letters* **20**, 57–68
707 (1999).
- 708 ⁴³N. J. Tustison, B. B. Avants, P. A. Cook, Y. Zheng, A. Egan, P. A. Yushkevich, and
709 J. C. Gee, “N4itk: Improved n3 bias correction,” *Ieee Transactions on Medical Imaging*
710 **29**, 1310–1320 (2010).
- 711 ⁴⁴N. L. of Medicine, “Insight segmentation and registration toolkit (itk),”
712 <http://www.itk.org/>.
- 713 ⁴⁵A. Gubern-Merida, M. Kallenberg, R. Marti, and N. Karssemeijer, “Segmentation of the
714 pectoral muscle in breast mri using atlas-based approaches,” *Medical image computing and*
715 *computer-assisted intervention : MICCAI ... International Conference on Medical Image*
716 *Computing and Computer-Assisted Intervention* **15**, 371–8 (2012).
- 717 ⁴⁶L. Wang, K. Filippatos, O. Friman, and H. K. Hahn, “Fully Automated Segmentation of
718 the Pectoralis Muscle Boundary in Breast MR Images,” in *MEDICAL IMAGING 2011:*
719 *COMPUTER-AIDED DIAGNOSIS*, Proceedings of SPIE, Vol. 7963, edited by Summers,
720 RM and VanGinneken, B (2011).
- 721 ⁴⁷A. Gubern-Mérida, L. Wang, M. Kallenberg, R. Marti, H. K. Hahn, and N. Karssemeijer,
722 “Breast segmentation in mri: quantitative evaluation of three methods,” *Medical Imaging*
723 *2013: Image Processing* **8669** (2013).
- 724 ⁴⁸L. D. Griffin, “The second order local-image-structure solid,” *IEEE Transactions on Pat-*
725 *tern Analysis and Machine Intelligence* **29**, 1355–1366 (2007).
- 726 ⁴⁹C. S. Poon, M. J. Bronskill, R. M. Henkelman, and N. F. Boyd, “Quantitative magnetic
727 resonance imaging parameters and their relationship to mammographic pattern,” *Journal*
728 *of the National Cancer Institute* **84**, 777–781 (1992).
- 729 ⁵⁰H. Song, X. Cui, and F. Sun, “Breast tissue 3d segmentation and visualization on mri,”
730 *International journal of biomedical imaging* **2013**, 859746–859746 (2013).
- 731 ⁵¹K. Van Leemput, F. Maes, D. Vandermeulen, and P. Suetens, “Automated model-based
732 tissue classification of mr images of the brain,” *IEEE Transactions on Medical Imaging*
733 **18**, 897–908 (1999).
- 734 ⁵²A. E. W. Ledger, E. D. Scurr, J. Hughes, A. Macdonald, T. Wallace, K. Thomas, R. Wilson,
735 M. O. Leach, and M. A. Schmidt, “Comparison of dixon sequences for estimation of percent

⁷³⁶ breast fibroglandular tissue,” PLoS ONE **11**, e0152152 (2016).